Extending the Modular Earth Submodel System (MESSy v2.55) model hierarchy: The ECHAM/MESSy idealized (EMIL) model set-up

Hella Garny[1,2], Roland Walz[1], Matthias Nützel[1], and Thomas Birner[2]

[1]Deutsches Zentrum für Luft- und Raumfahrt (DLR), Institut für Physik der Atmosphäre, Oberpfaffenhofen, Germany
[2]Ludwig Maximilians University of Munich, Meteorological Institute Munich, Munich, Germany

Correspondence: Hella Garny (Hella.Garny@dlr.de)

Abstract. While models of the Earth system gain more and more complexity, a need emerges to establish model hierarchies and to utilize simplified models to improve process understanding. The Modular Earth Submodel System (MESSy) was developed with the aim to provide an environment to allow for model configurations and set-ups of varying complexity, and as of now the hierarchy reaches from a chemical box model to the full coupled ECHAM/MESSy Atmospheric Chemistry (EMAC) Chemistry-Climate model. In the current study, we present and document the development of a new simplified set-up within the ECHAM/MESSy model, namely the dry dynamical core model set-up ECHAM/MESSy IdeaLized (EMIL). The set-up is achieved by the implementation of a new submodel for relaxation of temperature and horizontal winds to given background values (the RELAX submodel), which replaces all other "physics" submodels in the EMIL set-up. The RELAX submodel incorporates options to set the needed parameters (e.g., equilibrium temperature, relaxation time and damping coefficient) to functions used frequently in the past (given by Held and Suarez, 1994; Polvani and Kushner, 2002). Test simulations with the EMIL model set-up show that results from earlier studies with other dry dynamical core models are reproduced under same set-ups. Furthermore, modifications to the previously used set-ups are tested, with the following main findings: 1) lowering the equilibrium temperature in the lower stratosphere at winter polar high latitudes to more realistic values (i.e., below observed temperatures) results in high latitudes temperature profiles in the model closer to observations, and 2) when replacing the idealized topography to generate planetary waves by mid-tropospheric wave-like heating (as suggested in a previous study), the response of the tropospheric jet to changes in the equilibrium temperature is strongly damped, indicating that the wave-like heating has to be used with care. As application examples, we present simulations with simplified chemistry to study the impact of dynamical variability and idealized changes on tracer transport, and simulations of idealized monsoon circulations forced by localized heating. The ability to simulate dynamical systems and to incorporate passive and chemical active tracers in the EMIL set-up demonstrates the potential for future studies of tracer transport in the idealized dynamical model.

1 Introduction

Earth system models incorporate more and more processes and compartments to enable the simulation of the coupled climate system and thus produce the best possible climate projections. However, with models gaining more and more complexity, it

becomes difficult to isolate and understand the role of individual processes. This "gap between simulation and understanding in climate modeling" was pointed out in the paper by Held (2005), and it was suggested that the way forward is to work with a hierarchy of models with reduced to full complexity. Two recent overview papers (Jeevanjee et al., 2017; Maher et al., 2018) give surveys of current concepts and activities in building hierarchical model systems.

5   The basic concept in constructing a simplified model is to include only those processes, that are (absolutely) relevant for the question to be addressed. Thereby, the behavior of those processes can be isolated in an idealized environment, and the interaction of the limited number of processes chosen can be investigated.

    A frequently used idealized model set-up for studying global large-scale dynamics is the dry dynamical core model described by Held and Suarez (1994, HS94 hereafter) . While originally developed and used for testing dynamical model cores, the

10 elegance of the model makes it an ideal tool for dynamical process studies, and it is widely used for this purpose (see Maher et al., 2018, for a review of applications). The HS94 model set-up uses the full dynamical core of a GCM, but replaces all physics by relaxation towards a prescribed equilibrium temperature and by Rayleigh friction to damp winds at the surface and the upper model levels. Thus, with this model set-up the thermodynamic forcing of the atmosphere can be easily modified and the response of the large-scale circulation to those isolated modifications can be studied. Examples are changes in equilibrium

15 meridional temperature gradient or thermal damping time scale (Gerber and Vallis, 2007), or changes in surface friction (Chen et al., 2007). The functions for the equilibrium temperature and relaxation coefficients suggested in HS94 are widely used, and the HS94 model set-up was extended to study the dynamics of the stratosphere-troposphere system by modifying the equilibrium temperature of the stratosphere (Polvani and Kushner, 2002, PK02 hereafter) and later by adding topography to include planetary wave generation that is essential for the stratospheric circulation (Gerber and Polvani, 2009). This model

20 set-up was used among others to study stratosphere-troposphere coupling (Gerber and Polvani, 2009), the structure of the Brewer-Dobson circulation (Gerber, 2012), and the circulation's response to idealized heating resembling climate change (e.g., Butler et al., 2010; Wang et al., 2012). Recently, it was suggested that the forcing of planetary waves can also be achieved by inserting diabatic heating in the mid- to upper troposphere (Lindgren et al., 2018), which leads to a similar climatology as the topographically forced simulations, but to changes in the sudden stratospheric warming properties.

25   Beyond the purely dry dynamical core models, which are useful to study aspects of the global circulation, a question that motivates to include another level of complexity, is the interaction of moisture with large-scale dynamics, either by latent heat release or by its role as greenhouse gas. Frierson et al. (2006) expanded the dry dynamical core ("Held-Suarez") model by adding moisture and convection with latent heat release to the model, including simplified (gray) radiation that is insensitive to water vapor, thus tackling the question of the role of latent heat release for large scale dynamics. In a step further, Jucker and

30 Gerber (2017) included a full radiation scheme to capture the role of water vapor as radiative active gas (but neglecting clouds and aerosol forcing in the radiative calculation).

    Several initiatives are currently under way to build modeling frameworks with set-ups of varying complexity within the same model system (Vallis et al., 2018; Polvani et al., 2017), an approach that will advance both the usability of idealized models as well as the connectedness of the simple and the more complex model set-ups. In the same spirit, the Modular Earth Sub-

35 model System (MESSy, Jöckel et al., 2005) was developed explicitly with the goal to provide "a framework for a standardized,

bottom-up implementation of Earth System Models (or parts of those) with flexible complexity" (see https://www.messy-interface.org/). The motivation of the MESSy framework was originally to incorporate chemical processes of varying complexity into an Earth System model. The system includes model configurations ranging from a box model of atmospheric chemistry (Sander et al., 2019) to the complex chemistry-climate model ECHAM/MESSy Atmsopheric Chemistry (EMAC),

5   coupled to a deep ocean model (Jöckel et al., 2016). An illustration of a selection of available model complexities is shown in Fig. 1, as function of the complexity in physical processes/ compartments included (horizontal axis) and of the complexity of atmospheric chemical processes included (vertical axis). The lowest complexity on the chemical axis are prescribed concentrations for radiative active species (e.g., ozone), followed by a simplified parametrization to include effects of methane oxidation on stratospheric water vapor. The chemistry module MECCA (Sander et al., 2019) contains a large set of reactions relevant in

10   the troposphere and stratosphere, but it can be configured to the user's needs by choosing any subset of reactions, thus allowing for simplified to very comprehensive chemical set-ups. The chemical calculations can be performed as a box model (Sander et al., 2019), or within a full general circulation model either without feedback between dynamics and chemistry (the so-called "Quasi Chemistry-Transport Model" (QCTM), see Deckert et al., 2011) or with feedback, i.e., as full chemistry-climate model (Jöckel et al., 2006; Jöckel et al., 2010, 2016). Besides the prescribed sea surface temperature set-up, a mixed-layer ocean

15   (Dietmüller et al., 2014) or a full ocean model (Pozzer et al., 2011) can be used.

One advantage of the MESSy framework is its modular nature, i.e., individual processes are implemented as independent submodels that can be easily exchanged or complemented by new processes, and each submodel can be easily switched on or off (by namelist choice). Therewith, the hurdle of code modifications to build a model tailored to the necessary complexity is rather low. Moreover, the design of the model system allows to create model hierarchies in which the same code can be

20   used in a simple model set-up as well as in the full Earth-System model, thus any developments in model components can be transferred easily up- and downward in the model hierarchy.

As stated above, the nature of the hierarchy that is to be constructed depends on the scientific question at hand. Our aim is to study the large-scale dynamical variability of the stratosphere-troposphere system and its response to idealized forcings, and furthermore the impact of dynamical variability and changes on transport of passive and chemically active trace gases. To

25   achieve this goal, the most suited model set-up is a dry dynamical core model with the utilities for tracer transport and a set of chosen chemical reactions (simplified to the needs of the user). The implementation of such a model set-up within the MESSy framework is documented in the current paper.

Another step in constructing a consistent model hierarchy of chemistry-dynamical coupling would be to allow the anomalies of chemically and radiative active tracers caused by transport to feedback on the dynamics. This would require radiative

30   calculations depending on the actual tracer concentrations. While this expansion of the idealized set-up will be subject of future work, we note here that all necessary components are available already in the MESSy framework: the radiation scheme from the full EMAC model (Dietmüller et al., 2016) can be used with setting the input to either the online simulated values of the trace gas of interest (i.e., ozone), while the other relevant species can be set to climatological values (e.g., water vapor) or zero (e.g., clouds and aerosols). The envisioned model set-up, basically an idealized "chemistry-dynamical model", would thus
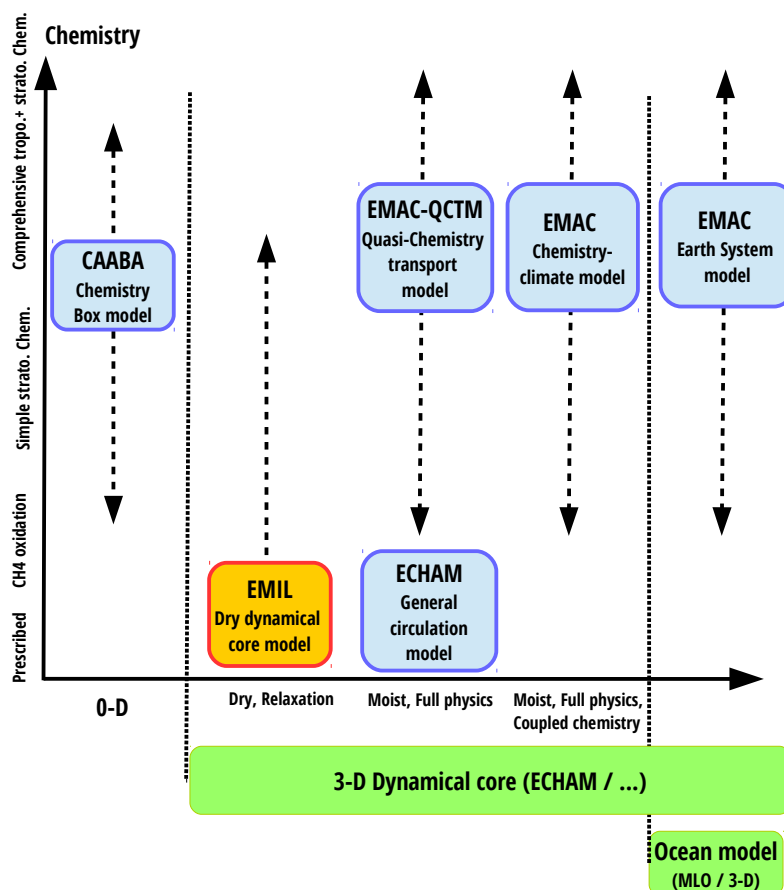
Figure 1. Schematic of the MESSy model hierarchy with existing (blue) model set-ups and the model set-up described in this paper (red). Model set-ups are displayed as function of their complexity in dynamics/physics/compartments (horizontal axis) versus complexity in chemical mechanism (vertical axis).

consist of a dry dynamical core with thermodynamic forcing by an idealized prescribed latent heating and radiative calculations that are dependent on the chemical species of interest (e.g., ozone).

In this paper, we document the implementation of the dynamical core set-up within MESSy and its performance. The implementation is achieved by adding a simple submodel for Newtonian cooling and Rayleigh friciton, that replaces the complex physics (see Sec. 2 and the supplement for technical details including a user manual). Next to standard test cases

with the forcing as in Held and Suarez (1994) and its stratospheric extension (Polvani and Kushner, 2002, see Sec. 3), we test several modifications to those set-ups, most importantly a modification of the equilibrium temperatures in the winter high latitudes that leads to more realistic temperature profiles in the lower stratosphere (Sec. 4). We further test the sensitivity of the simulated dynamics to the generation of large-scale waves by zonally asymmetric heating instead of idealized topography, as

5 suggested recently by Lindgren et al. (2018).

Finally, we present two application examples of the model: first, we present simulations including a small set of chemical reactions (namely photolysis of Chlorofluorocarbons) and demonstrate the potential of the model to study the role of dynamical variability and idealized changes on tracer transport (Sec. 5.1). Secondly, the simulation of an upper tropospheric anticyclone forced by idealized locally constrained heating that resembles the Asian monsoon anticyclone is presented in Sec. 5.2.

10 2 Model description

The ECHAM/MESSy IdeaLized (EMIL) model set-up is based on MESSy version 2.55 (Jöckel et al., 2006; Jöckel et al., 2010, 2016). In the idealized model set-up, all physics (radiation, clouds and surface processes) are switched off, and are replaced by the newly implemented submodel "RELAX", that relaxes the variables temperature and horizontal winds to background values. The submodel RELAX is described in the next subsection. Technical details of the model set-up (namelist choices etc.)

15 and implementation are provided in the supplement.

2.1 The submodel RELAX

The submodel RELAX calculates (1) Newtonian cooling which relaxes the temperature towards a given equilibrium temperature with a given relaxation time scale, (2) Rayleigh friction which relaxes the horizontal wind towards zero with a given damping coefficient, and (3) additional diabatic heating over selected regions. The three processes are switched on/off via

20 namelist parameters (in relax.nml, see Supplement).

The submodel is called from the physics routine *physc* through *messy_physc*. The full call tree including all subroutines is provided in the supplement.

2.1.1 Newtonian cooling

The temperature tendency calculated by Newtonian cooling is given by

$$25 \quad \frac{\delta T}{\delta t} = -\kappa(T - T_{\mathrm{equ}}) \tag{1}$$

where κ is the inverse relaxation time scale, T the local temperature calculated by the model, and T_{equ} the prescribed equilibrium temperature.

The inverse relaxation time scale κ and the equilibrium temperature T_{equ} have to be specified in the model set-up via the RELAX namelist file (relax.nml, including the "coupling" (CPL) namelist in which all options are set). There are three options:

30 (1) Set κ and/or T_{equ} to a constant value specified in the namelist. This option is physically of little use and is implemented

for test purposes only. (2) Choose one of the implemented functions for κ and/or T_{equ}. Those options are described below. (3) Set κ and/or T_{equ} to a field that is imported from an external file (via import.nml). The imported fields are interpolated to the current pressure profile at each time step within the RELAX submodel.

The implemented functions (option (2)) for κ and T_{equ} are either those given by HS94 (option 'HS'), or those given by PK02

5 (option 'PK'), but with the possibility of extensions. Note that κ in 'PK' and 'HS' are identical.

The functions for the 'HS' set-up, as defined by Held and Suarez (1994), are

$$T_{\mathrm{equ}}^{\mathrm{HS}} = \max\left\{ T_{\mathrm{top}}, \left[T_0 - \delta_y \sin^2\phi - \epsilon\sin\phi - \delta_z \log\left(\frac{p}{p_0}\right)\cos^2\phi \right]\left(\frac{p}{p_0}\right)^k \right\}, \tag{2}$$

$$\kappa = \kappa_{\mathrm{a}} + (\kappa_{\mathrm{s}} - \kappa_{\mathrm{a}})\max\left(0, \frac{p/p_s - \sigma_{\mathrm{b}}}{1 - \sigma_{\mathrm{b}}}\right)\cos^4\phi \tag{3}$$

10 where ϕ is the geographical latitude and p the local pressure. All constants can be set via namelist entries, with defaults set to the values given in HS94 ($T_{\mathrm{top}} = 200\,\mathrm{K}$, $T_0 = 315\,\mathrm{K}$ $\delta_y = 60\,\mathrm{K}$, $\delta_z = 10\,\mathrm{K}$, $k = R/c_p = 2/7$, $p_0 = 1013.25\,\mathrm{hPa}$, $\kappa_{\mathrm{a}} = (40\,\mathrm{days})^{-1}$, $\kappa_{\mathrm{s}} = (4\,\mathrm{days})^{-1}$ and $\sigma_{\mathrm{b}} = 0.7$). p_s is the current surface pressure. The parameter h_{fac}, that is set in the namelist, controls the hemispheric asymmetry: If h_{fac} is zero, the equilibrium temperature is symmetric between the hemispheres (i.e., $\epsilon = 0$). If $h_{\mathrm{fac}} \neq 0$, then $\epsilon = \mathrm{sign}(h_{\mathrm{fac}}) \times 10\,\mathrm{K}$, i.e., the sign of h_{fac} determines which hemisphere is the winter hemisphere

15 (positive h_{fac}: northern hemispheric winter, negative h_{fac}: southern hemispheric winter).

The equilibrium temperature in the PK set-up is similar to the one of HS in the troposphere, but uses the following function in the stratosphere above a given transition pressure $p_{\mathrm{T}}(\phi)$:

$$T_{\mathrm{equ}}^{\mathrm{PK}}(\phi, p) = \begin{cases} \max\left\{ T_{\mathrm{US}}(p_{\mathrm{Ts}}), \left[T_0 - \delta_y \sin^2(\phi) - \epsilon\sin(\phi) - \delta_z \log\left(\frac{p}{p_0}\right)\cos^2(\phi) \right]\left(\frac{p}{p_0}\right)^k \right\} & \text{for } p \geq p_{\mathrm{T}}(\phi) \\ \left[1 - W(\phi)\right]T_{\mathrm{US}}(p) + W(\phi)\,T_{\mathrm{US}}(p_{\mathrm{Ts}})\left(\frac{p}{p_{\mathrm{T}}(\phi)}\right)^{\frac{R\gamma}{g}} & \text{for } p < p_{\mathrm{T}}(\phi) \end{cases} \tag{4}$$

The stratospheric temperature profile is based on the US standard atmosphere temperature profile $T_{\mathrm{US}}(p)$ in the summer

20 hemisphere and exhibits a temperature decrease with lapse rate γ in the winter hemisphere representing the region of the polar vortex. This transition is performed by the weighting function

$$W(\phi) = \frac{1}{2}\left[1 + \mathrm{sign}(h_{\mathrm{fac}})\tanh\left(\frac{\phi - \phi_0}{\delta\phi}\right)\right]. \tag{5}$$

The smooth transition between tropospheric and stratospheric temperatures is ensured by bounding the tropospheric temperature to the temperature in the transition region $T_{\mathrm{US}}(p_{\mathrm{Ts}})$.

25 As an extension to the original PK set-up, we include the possibility to vary the transition pressure from summer to winter hemisphere, using the weighting function $W(\phi)$:

$$p_{\mathrm{T}}(\phi) = (p_{\mathrm{Tw}} - p_{\mathrm{Ts}})W(\phi) + p_{\mathrm{Ts}} \tag{6}$$

where p_{Ts} and p_{Tw} are the transition pressures over the summer and winter hemisphere, respectively. Again, all constants can be set in the namelist with default values $T_0 = 315\,\mathrm{K}$, $\delta_y = 60\,\mathrm{K}$, $\delta_z = 10\,\mathrm{K}$, $k = R/c_p = 2/7$, $p_0 = 1013.25\,\mathrm{hPa}$, $|\epsilon| = 10\,\mathrm{K}$,
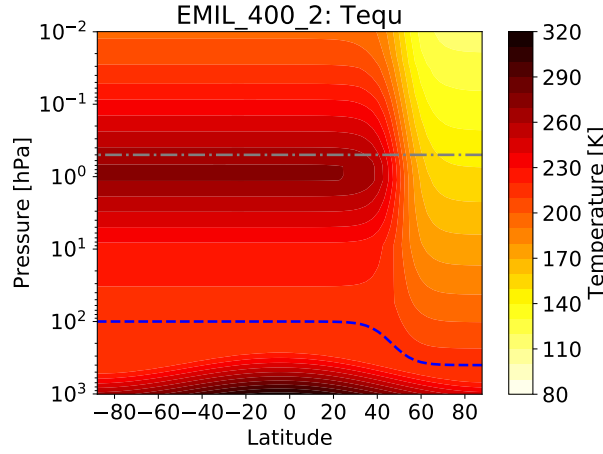
Figure 2. Equilibrium temperature (in K) for $p_\mathrm{Tw} = 400\,\mathrm{hPa}$ and $\gamma = 2\,\mathrm{K\,km}^{-1}$ together with the transition pressure $p_\mathrm{T}(\phi)$ (blue dashed line) and the pressure above which damping sets in (gray dashed-dotted line).

$|\phi_0| = 50$, $\delta\phi = 10$, $h_\mathrm{fac} = 1$, $\gamma = 4\,\mathrm{K/km}$, $p_\mathrm{Ts} = 100\,\mathrm{hPa}$ and $p_\mathrm{Tw} = 100\,\mathrm{hPa}$. These default values correspond to the original PK02 set-up with constant transition pressure $p_\mathrm{T}(\phi) \equiv 100\,\mathrm{hPa}$.

In the following, only the polar vortex lapse rate γ and the transition pressure p_Tw over the winter high latitudes are varied, whereas $p_\mathrm{Ts} = 100\,\mathrm{hPa}$ is held constant. Fig. 2 shows the zonally symmetric equilibrium temperature for $p_\mathrm{Tw} = 400\,\mathrm{hPa}$ and

5   $\gamma = 2\,\mathrm{K\,km}^{-1}$.

2.1.2   Rayleigh friction

Horizontal winds are relaxed to zero (i.e., damped) with a given damping coefficient k_damp by:

$$\frac{\delta u}{\delta t} = -k_\mathrm{damp} u$$
$$\frac{\delta v}{\delta t} = -k_\mathrm{damp} v \qquad (7)$$

As for the Newtonian cooling, the damping coefficient can be selected via the namelist with the same three options (i.e.,

10   constant, implemented function, or imported externally). The implemented functions that can be chosen are:

1) Damping of the surface layer as specified by HS94 (option 'HS'):

$$k_\mathrm{damp} = k_\mathrm{max} \max\left(0, \frac{\frac{p}{p_s} - \sigma_0}{1 - \sigma_0}\right) \qquad (8)$$

with default values $k_\mathrm{max} = 1.16 \times 10^{-5}\,\mathrm{s}^{-1}$, $\sigma_0 = 0.7$ and p_s the current surface pressure.

2) Damping of a layer at the model top as specified by PK02 (option *'PK'*):

$$k_{\mathrm{damp}} = \begin{cases} 0 & \text{for } p > p_{\mathrm{sp}} \\ k_{\mathrm{max}} \left(1.0 - \frac{p}{p_{\mathrm{sp}}}\right)^2 & \text{for } p \leq p_{\mathrm{sp}} \end{cases} \tag{9}$$

with default values $k_{\mathrm{max}} = 2.3148 \times 10^{-5}\,\mathrm{s}^{-1}$ and $p_{\mathrm{sp}} = 0.5\,\mathrm{hPa}$.

3) Damping of a layer at the model top with the function as implemented in the original ECHAM code (option *'EH'*):

$$k_{\mathrm{damp}} = \begin{cases} 0 & \text{for } i_{\mathrm{lev}} > i_{\mathrm{lev}}^{sp} \\ k_{\mathrm{drag}} c^{i_{\mathrm{lev}}^{sp} - i_{\mathrm{lev}}} & \text{for } i_{\mathrm{lev}} \leq i_{\mathrm{lev}}^{sp} \end{cases} \tag{10}$$

where i_{lev} is the number of the hybrid level counted from the top of the model for a vertical resolution of L90MA. Thus, the drag k_{drag} is enhanced by a factor of c for each level going upward. Default values are $c = 1.5238$, $k_{\mathrm{drag}} = 5.02 \times 10^{-7}\,\mathrm{s}^{-1}$ and $i_{\mathrm{lev}}^{sp} = 10$, corresponding to a pressure of $0.43\,\mathrm{hPa}$ for the L90MA vertical resolution. If the model is run at a different vertical resolution, the damping coefficients are first calculated according to Eq. 10 for L90MA, and then interpolated to the current vertical levels.

As damping at the model surface (option 1) and at the upper layers (options 2 or 3) are complementary, more than one option can be chosen. In this case, the chosen profiles of k_{damp} are added.

2.1.3 Diabatic heating routines

In addition to the zonally symmetric temperature tendency calculated by Newtonian cooling, additional temperature tendencies (diabatic heating) can be employed. Currently, three options are implemented, one function for zonal mean heating (*tteh_cc_tropics*), a wave-like heating varying with longitude λ (*tteh_waves*) and a function for localized heating (*tteh_mons*).

The zonal mean diabatic heating (*tteh_cc_tropics*) is one of the tropical heating functions given by Butler et al. (2010), and reads

$$Q_0(\lambda, \phi, p) = q_0 \exp\left[-\frac{1}{2}\left(\frac{\phi - \phi_0}{\sigma_\phi}\right)^2 - \frac{1}{2}\left(\frac{p/p_s - z_0}{\sigma_z}\right)^2\right] \tag{11}$$

with p_s being the surface pressure and default values of $q_0 = 0.5\,\mathrm{K/day}$, $\phi_0 = 0°\mathrm{N}$, $\sigma_\phi = 0.4 \cdot 180°/\pi$, $z_0 = 0.3$ and $\sigma_z = 0.11$ as used by Butler et al. (2010).

The temperature tendency *tteh_waves*, used here for the generation of planetary waves introduced by Lindgren et al. (2018), reads

$$Q_0(\lambda, \phi, p) = \begin{cases} q_0 \sin(m\lambda) \exp\left[-\frac{1}{2}\left(\frac{\phi - \phi_0}{\sigma_\phi}\right)^2\right] \sin\left(\pi \frac{\log(p/p_{\mathrm{bot}})}{\log(p_{\mathrm{top}}/p_{\mathrm{bot}})}\right) & \text{for } p_{\mathrm{top}} \leq p \leq p_{\mathrm{bot}}, \\ 0 & \text{otherwise} \end{cases} \tag{12}$$

with default values $q_0 = 6\,\mathrm{K/day}$, $m = 2$, $\phi_0 = 45°\mathrm{N}$, $\sigma_\phi = 0.175 \cdot 180°/\pi$, $p_\mathrm{bot} = 800\,\mathrm{hPa}$ and $p_\mathrm{top} = 200\,\mathrm{hPa}$ as used by Lindgren et al. (2018).

The other additional temperature tendency, *tteh_mons*, allows to impose a localized heat source. The effect of localized heat sources has been investigated in a couple of studies (e.g., Gill, 1980; Schubert and Masarik, 2006; Siu and Bowman, 2019)

5 and we will use localized heating to produce monsoon-like anticyclones in Sec.5.2 (hence the name *tteh_mons*). The function describing the localized heating field is given as:

$$Q_{loc}(\lambda, \phi, p, t) = Q_{temp}(t) Q_{pres}(p) Q_{lat}(\phi) Q_{lon}(\lambda). \tag{13}$$

Here, the individual factors are used to describe the temporal and spatial (horizontal and vertical) dependence of the heating function. The temporal evolution of the heating is given by:

10 $$Q_{temp}(t) = \begin{cases} \frac{t}{t_s} \times (q_0 + q_{temp}\, sin(2\pi \frac{t}{\delta t})) & \text{for } 0 \leq t \leq t_s, \\ 1 \times (q_0 + q_{temp}\, sin(2\pi \frac{t}{\delta t})) & \text{otherwise.} \end{cases} \tag{14}$$

To slowly increase the heating after the start of the simulation a spin up factor of $\frac{t}{t_s}$ is included until the end of the spin up time (t_s). After the spin up time (t_s) the temporal variation of the heating is only given by a periodic oscillation (period δt) with amplitude (q_{temp}) around a constant base heating (q_0).

In the vertical the heating is assumed to be of the same form as in Eq. (12), i.e.:

15 $$Q_{pres}(p) = \begin{cases} sin(\pi \frac{log(p/p_{bot})}{log(p_{top}/p_{bot})}) & \text{for } p_{top} \leq p \leq p_{bot}, \\ 0 & \text{otherwise.} \end{cases} \tag{15}$$

Here, p_{bot} and p_{top} denote the maximum and minimum pressure to which the heating is confined in the vertical. The latitudinal dependence for $\phi \in [-90, 90]$ follows the function suggested by Schubert and Masarik (2006, their Eq. 4.1), and is given as

$$Q_{lat}(\phi) = exp(-(\frac{\phi - \phi_0}{\delta\phi})^2) \tag{16}$$

Finally, the longitudinal dependence for $\lambda \in [0, 360)$ is given by

20 $$Q_{lon}(\lambda) = \begin{cases} 0.5(1 + cos(\pi \frac{g(\lambda, \lambda_0)}{\delta\lambda})) & \text{if } g(\lambda, \lambda_0) \leq \delta\lambda \\ 0 & \text{otherwise} \end{cases} \tag{17}$$

where $g(\lambda, \lambda_0) = min((\lambda - \lambda_0)\, mod(360), (\lambda_0 - \lambda)\, mod(360))$ and the modulo function $mod(360)$ maps $\mathbb{R}$ to $[0, 360)$, i.e. the function returns the smallest angle between the longitude λ and the central longitude λ_0 with accounting for the crossing of the $0°$ line. Again the longitudinal function is based on the heating described by Schubert and Masarik (2006, their Eq. 4.1). However, as Schubert and Masarik (2006) were aiming to investigate the Madden-Julian-Oscillation, they included a movement

25 of the localized heat source, which we do not include here (i.e., we use their equation with propagation speed 0). Overall this heating structure is similar to other idealized heatings used for studying monsoon anticyclones (e.g., Siu and Bowman, 2019).
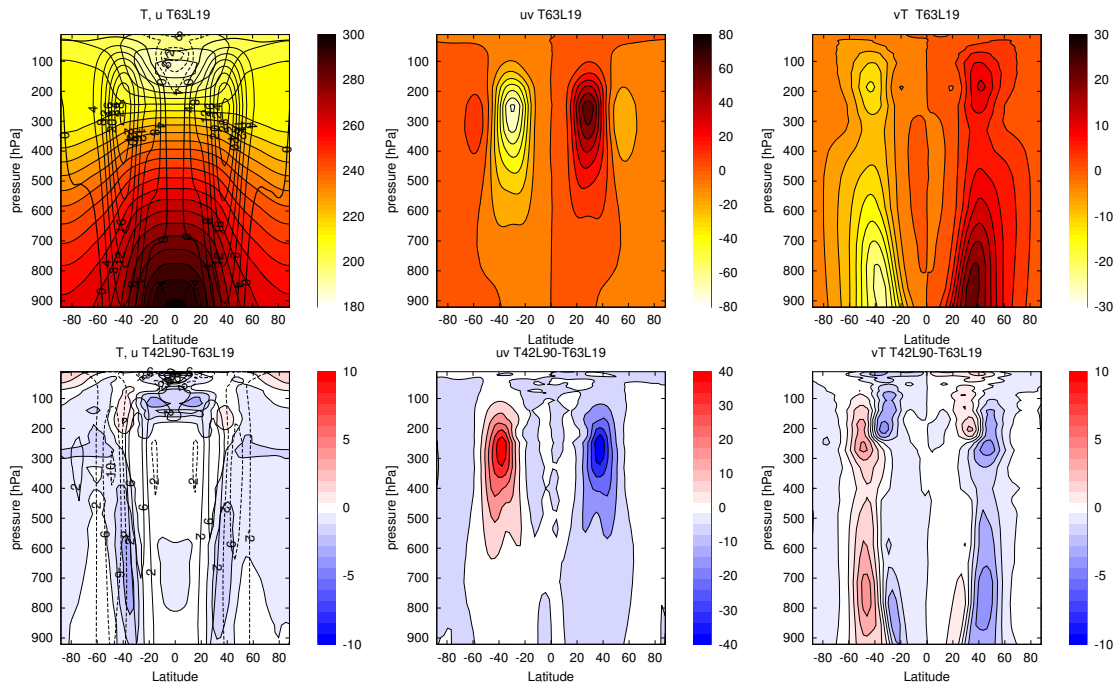
Figure 3. Top: Results from a HS simulation at T63L19 resolution, showing mean temperature [K] and zonal mean zonal wind [m s^{-1}] (left), mean eddy momentum fluxes [m^2 s^{-2}] (middle) and mean eddy heat fluxes [mK s^{-1}] (right) averaged over 1000 days (after spin-up of 450 days). Bottom: As above, but difference of a simulation at T42L90MA resolution to the T63L19 simulation.

3   Model test cases

In this section, results obtained with the EMIL set-up are compared to results of earlier studies with identical set-ups (both with the Held-Suarez set up, Sec. 3.1 and the Polvani-Kushner set-up, Sec. 3.2) to test whether the EMIL implementation is able to reproduce those earlier studies. If not mentioned otherwise, the simulations are performed for 1825 days, with the first

5   300 days considered as spin-up and not included in the analysis.

3.1   Held-Suarez forcing

Results of idealized ECHAM5 simulations with the Held-Suarez set-up were previously presented in the study by Wan et al. (2008). We ran a simulation with identical set-up and resolution (T63L19) to test whether our implementation of the Held-Suarez set-up with the same base model can reproduce the results of Wan et al. (2008). As shown in Fig. 3 the climatologies

10   of zonal wind, temperature and eddy fluxes are closely reproduced when compared to Fig. 1 of Wan et al. (2008). The wind jet maxima are identical at 28 ms^{-1}, as well as the eddy variance maxima (at 40 K^2).

In the remainder of the paper, a vertical resolution with high top (0.01 hPa) and with 90 levels will be used together with T42 as spectral resolution (one of the standard resolutions of EMAC, see Jöckel et al., 2016). The differences in the climatologies

between the T42L90MA and the T63L19 simulation (for the HS set-up) are shown in Fig. 3 (bottom). In agreement with results presented by Wan et al. (2008), there are shifts in the jet and a general reduction of eddy variance with lower horizontal resolution (which likely dominates over the effect of changed vertical resolution, see Wan et al., 2008). The issue of resolution sensitivity will not be touched further as it is not the subject of this paper, but it should be kept in mind that the T42 spectral

5   resolution is below the resolution of convergence (estimated to be T85L31 by Wan et al., 2008) for tropospheric eddy dynamics.

3.2   Polvani-Kushner set-up

In the study by PK02, an equilibrium temperature is introduced that enables the simulation of an active stratosphere with a polar vortex in the winter hemisphere.

As a test case, EMIL simulations are performed with identical forcing as in PK02, i.e., with the same choice of the prescribed

10   equilibrium temperature and the damping layer at the top of the model. The results for simulations with the polar temperature lapse rate γ set to 4 K km^{-1} are shown in Fig. 4 (bottom left). The polar vortex strength maximizes at around around 90 ms^{-1} for $\gamma = 4$, and at 30 ms^{-1} for $\gamma = 1$ (not shown), similar to the wind maxima shown in PK02. Also the structure of the polar vortex, and the subtropical jets agree well between our simulation and the ones presented by PK02. Based on the same model as used by PK02 (namely GFDL), Jucker et al. (2013) show climatologies of wind and temperature for the PK02 set-up

15   with $\gamma = 4$. The temperature climatology of the EMIL simulation with $\gamma = 4$ agrees well with the one shown by Jucker et al. (2013), with both models simulating a tropical lower stratospheric temperature minimum of 210 K and a pronounced minimum in temperature (T < 180 K) at the winter pole around 10 hPa. Note that when compared to the southern winter climatologies from ERA-Interim Reanalysis (Dee et al., 2011), as shown in Fig. 4 (top left), the winter high latitude temperature minimum is both too pronounced and too confined in altitude in the model. This issue that will be further discussed in Sec. 4.2.

20   For a second test case, we include the generation of planetary waves by an idealized topography, as proposed by Gerber and Polvani (2009). Fig. 4 (bottom right) shows the simulated climatologies with a wavenumber 2 (WN2) mountain with amplitude h = 3 km and $\gamma = 4$. Following Gerber and Polvani (2009), the mountain is centered at 45°N and falls off to zero at 25°N and 65°N. This set-up of the mountain was found to lead to most realistic simulation of the mean state of the polar vortex and its variability by Gerber and Polvani (2009). The resulting climatologies of zonal wind, with a polar vortex strength of about 50

25   ms^{-1}, and of temperature, with a minimum temperature over the winter pole at 10 hPa of around 180 K again closely reproduce the results by Gerber and Polvani (2009) and the equivalent simulation shown by Jucker et al. (2013). As in the case without topography, the winter high latitude temperature minimum is too pronounced and too confined in altitude when compared to northern winter climatologies in ERA-Interim (see Fig. 4, top right).

The variability of the polar vortex is diagnosed by the time-series of the zonal mean zonal wind at 10 hPa and 60N for the

30   PK simulation with $\gamma = 4$ and a WN2 mountain amplitude of h=3 km in Fig. 5 (black line). The polar vortex is highly variable with winds between -10 to 60 ms^{-1}, with sudden decreases in the wind speeds, known as sudden stratospheric warmings. The time series of the EMIL simulation presented here closely resembles that shown by Gerber and Polvani (2009) in terms of variability.
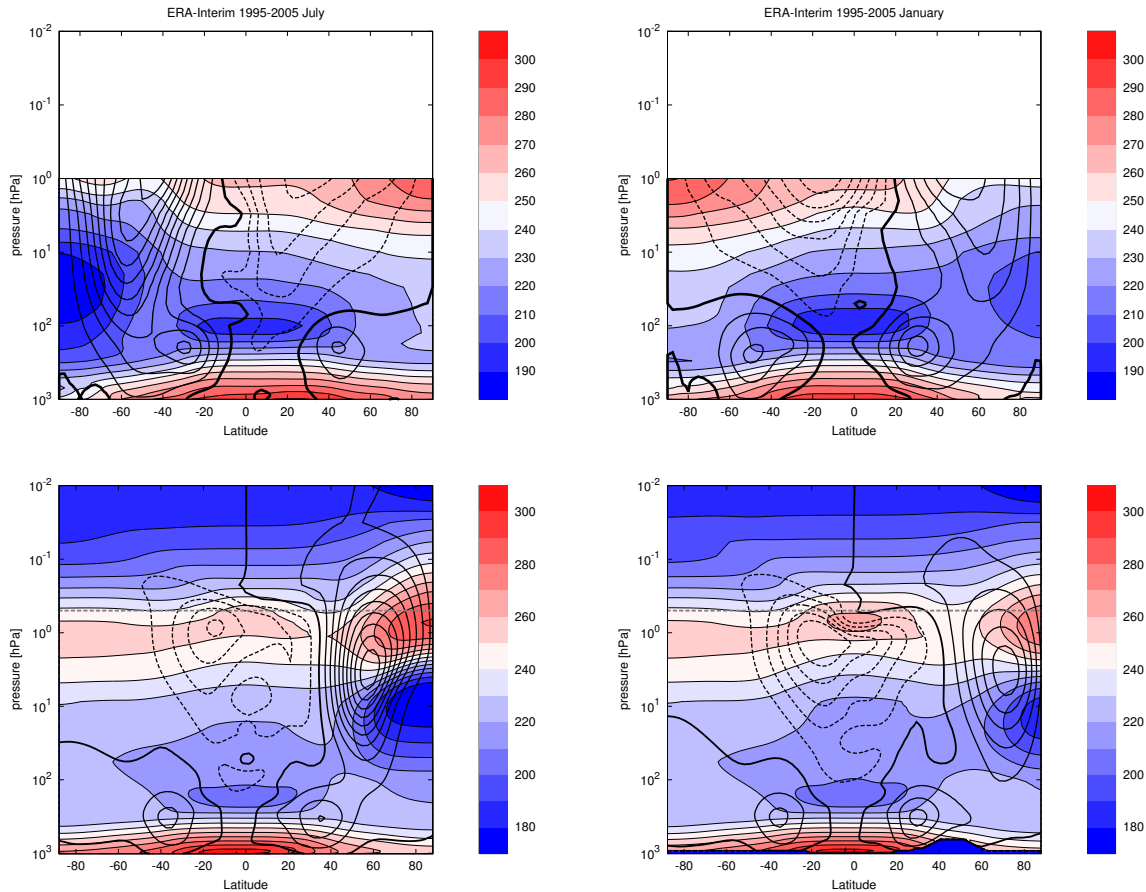
Figure 4. Climatologies of wind (black contours, contour interval 10 ms^{-1}, solid positive, dashed negative) and temperature [K] (colored contours) of (top left) July 1995 to 2004 of ERA-Interim, (top right) January 1995 to 2004 of ERA-Interim, (bottom left) an EMIL simulation with the PK02 set-up with $\gamma = 4$, and (bottom right) an EMIL simulation with the PK02 set-up with $\gamma = 4$ and with WN2 topography with h=3 km. The gray dashed horizontal lines in the EMIL climatologies mark the lower boundary of the damping layer.

Overall, the results of this section show that the EMIL set-up is able to reproduce earlier results of simulations performed with dynamical core models under same set-ups of T_{equ}, relaxation time, the damping layer and topographically generated planetary waves.

4 Sensitivity simulations

5   In this Section, the response of the climate to three different types of modifications are tested: (1) modifications in the shape of the upper atmospheric sponge layer, (2) modifications in the winter high-latitude equilibrium temperature profile, and (3) planetary wave generation by wave-like heating instead of topography.
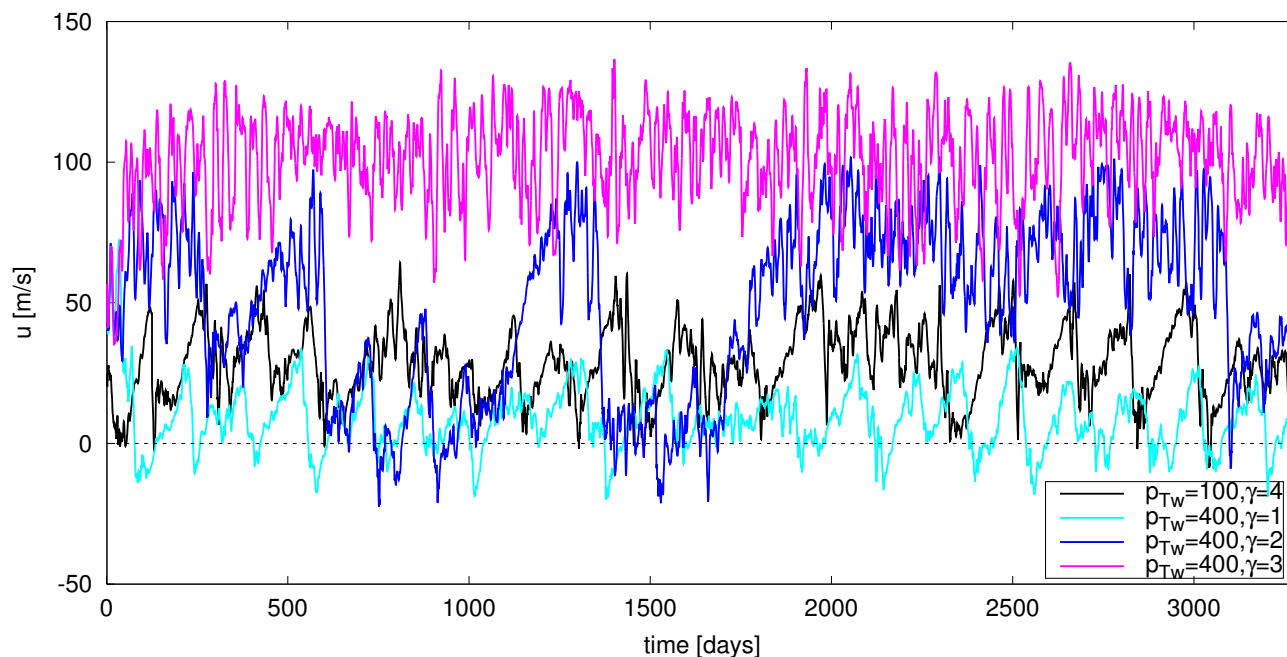
Figure 5. Timeseries of zonal mean zonal wind $[\mathrm{ms}^{-1}]$ at $10\,\mathrm{hPa}$ and $60°\mathrm{N}$ for different configurations of the PK set-up (see label).

4.1 Sensitivity to the shape of the upper atmospheric damping layer

The damping layer at levels above $0.5\,\mathrm{hPa}$ is included to account for the strong damping of winds that in the real atmosphere (or the full model) is due to drag by breaking gravity waves (GW). The simplified manner of damping the entire horizontal wind fields introduces a non-physical sink of momentum. When analyzing results obtained with the model, this has to be kept
5 in mind.

The damping layer as introduced by PK02 uses a damping coefficient that increases quadratically with decreasing pressure. The profile of the PK02 damping coefficient is shown in Fig. 6 together with the profile of zonal mean zonal wind tendencies due to parametrized gravity waves divided by the zonal mean wind (averaged over 40-60°S) from a model simulation with the full atmospheric EMAC set-up, i.e., an equivalent damping coefficient of the zonal mean wind by the parametrized GW drag.
10 The "damping" by GW drag increases with height exponentially rather than quadratically. Therefore, we argue that a damping coefficient with exponential increase mimics the net effects of parametrized GW drag better.

A sensitivity simulation is performed in which the damping coefficient in the upper model domain follows the exponential function given by Eq. (10) (option *EH*; this is the shape of the "sponge" layer originally implemented in the ECHAM model). The damping coefficient of this sensitivity simulation is shown in Fig. 6 as green line.
15 The simulated climate states with the two different set-ups of the sponge layer differ within the sponge layer (see Fig. 7), and differences in wind and temperature extend below the damping layer, but are negligible outside the winter high latitudes and
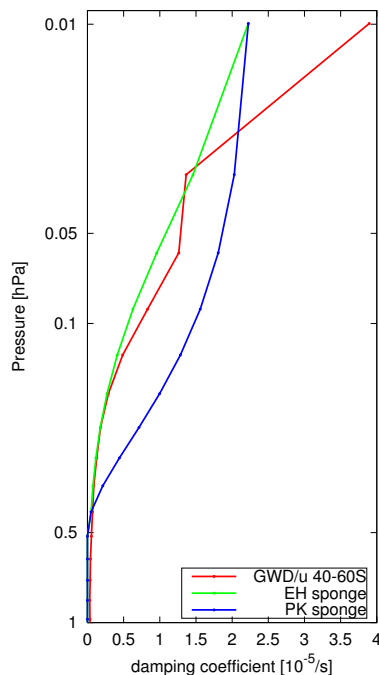
Figure 6. Damping coefficient $[s^{-1}]$ of the sponge layer in the "EH" (green) and in the PK02 set-up (blue) together with the "damping" of winds by GWD (i.e., -GWD/u) from an ECHAM simulation in July 2000 averaged over $40\text{-}60°$S (red).

below about 10 hPa. At high latitudes, an upward shift of the temperature maximum at the stratopause is found, as well as an increase in zonal winds, which maximizes at the lower bound of the damping layer. Since the *EH* sponge is weaker, the increase in zonal mean winds within the damping layer can be expected. The weaker sponge and changed zonal wind structure modifies planetary wave propagation (stronger upward propagation between from about 3 hPa upward, not shown), thus influencing

5 the mean climate also below the damping layer (decreased wave driving, leading to stronger zonal winds and lower polar temperatures). The effect of the modified damping coefficients is similar in simulations with WN2 topography (albeit with weaker absolute differences). As the exponentially increasing damping coefficient (*EH*) resembles the vertical structure of GW drag, and since for both, plane surface and idealized topography, the height at which the polar winter temperature profile reaches its maximum is more realistic in case of the *EH* damping layer (see Fig. 7 right), we chose to use the exponentially

10 increasing damping coefficient (*EH*) in the following as our reference set-up.

4.2 Sensitivity to modification of the equilibrium temperature in the winter high latitude lower stratosphere

The simulated winter high-latitude temperature profiles for EMIL simulations with *PK* set-up and WN2 topography are shown in Fig. 8 (left) for varying γ, compared to temperature profiles from the "SPARC" climatology (Randel et al., 2004; SPARC, 2002) for northern winter. The comparison of the simulations to the SPARC climatology reveals a positive temperature bias
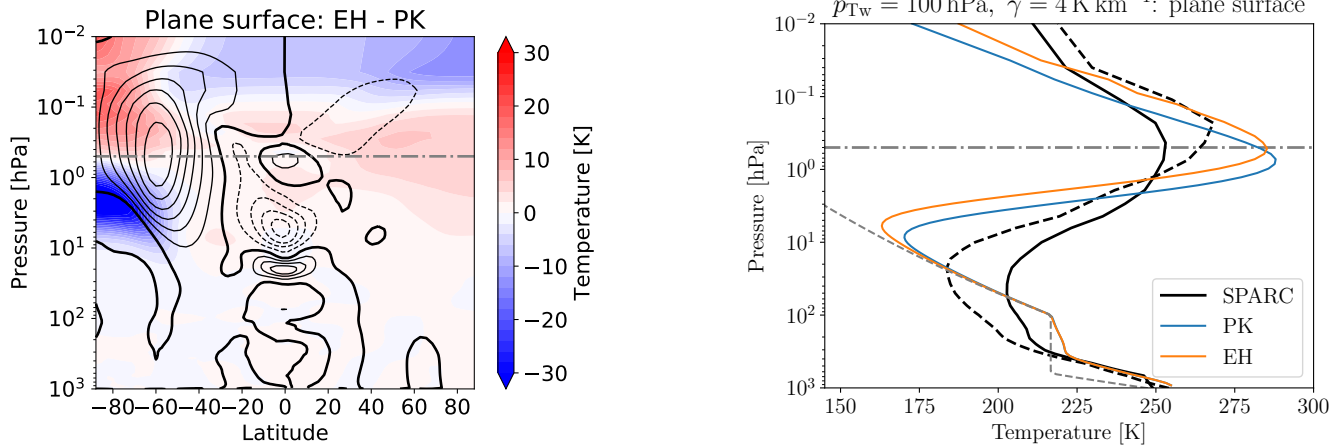
Figure 7. Left: Differences in zonal mean temperature [K] and zonal mean zonal wind [ms^{-1}] between a model simulation with exponentially increasing damping coefficient (*EH*) and a model simulation with quadratically increasing damping coefficient (*PK*) for $p_{\mathrm{Tw}} = 100\,\mathrm{hPa}$ and $\gamma = 4\,\mathrm{K\,km}^{-1}$ without topography. The temperature contour interval is $2\,\mathrm{K}$. The wind contour interval is $5\,\mathrm{m\,s}^{-1}$. Right: Polar winter temperature profiles of same model simulations averaged from $70°\mathrm{N}$ to $90°\mathrm{N}$, with temperature profiles from the SPARC climatology in northern hemispheric winter conditions (black solid line) and southern hemispheric winter conditions (black dashed line) as well as the equilibrium temperature profile (gray dashed line). The dash-dotted line marks the lower boundary of the sponge layer.

in the UTLS region of the winter high latitudes ($70°\mathrm{N}$ to $90°\mathrm{N}$), when using the standard *PK* set-up with a constant transition pressure of $p_{\mathrm{T}}(\phi) \equiv 100\,\mathrm{hPa}$. The positive temperature bias remains unchanged for different polar vortex lapse rates γ. Even for strong decreases of the equilibrium temperature above the $100\,\mathrm{hPa}$ level, the positive temperature bias in the UTLS region can not be compensated. This is essentially because the equilibrium temperature (shown in gray) already exceeds the

5 temperatures obtained from SPARC in that region. Due to the general-circulation transport of heat from the tropics to polar regions throughout the troposphere and stratosphere, the temperature bias even increases. Therefore, every simulation with $p_{\mathrm{Tw}} = 100\,\mathrm{hPa}$ necessarily has a too warm UTLS region in the winter high latitudes compared to the SPARC climatology (and compared to ERA-Interim reanalysis, see Fig. 4). The warm bias is associated with an unrealistic "step" in the temperature profile, forced by the constant equilibrium temperature profile up to $100\,\mathrm{hPa}$.

10 In order to approach a more realistic temperature profile in the UTLS region of the winter high latitudes, the transition pressure p_{Tw} is increased. The parameters p_{Tw} and γ are varied across $p_{\mathrm{Tw}} = 100$ to $450\,\mathrm{hPa}$ and $\gamma = 1$ to $4\,\mathrm{K\,km}^{-1}$. At $p_{\mathrm{Tw}} = 400\,\mathrm{hPa}$, all equilibrium temperatures in the polar winter UTLS region fall below the corresponding temperatures obtained from SPARC except the one for $\gamma = 1\,\mathrm{K\,km}^{-1}$ (see the right panel of Fig. 8). For the simulations with $\gamma = 3\,\mathrm{K\,km}^{-1}$ and $\gamma = 4\,\mathrm{K\,km}^{-1}$, the winter high-latitude temperatures are lower than the SPARC temperatures throughout the UTLS region,

15 and follow the equilibrium temperature up to about $30\,\mathrm{hPa}$. Above, the temperature increases strongly, reaching a maximum at around $0.7\,\mathrm{hPa}$. In contrast, the UTLS temperature in the simulation with $\gamma = 1\,\mathrm{K\,km}^{-1}$ is well above the corresponding equilibrium temperature in the UTLS, and the temperature maximum at around $0.5\,\mathrm{hPa}$ is weaker. The simulation with $\gamma =$
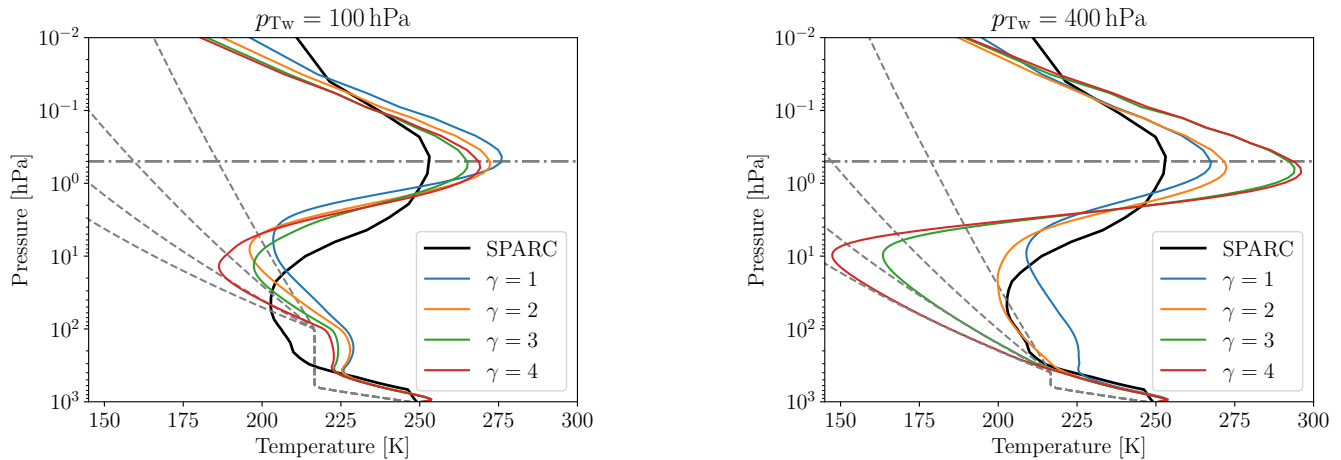
Figure 8. Polar winter temperature profiles of model simulations with WN2 topography of height $h = 3\,\mathrm{km}$ and different polar vortex lapse rates γ for $p_{\mathrm{Tw}} = 100\,\mathrm{hPa}$ (left) and $p_{\mathrm{Tw}} = 400\,\mathrm{hPa}$ (right), together with the temperature profiles obtained from the SPARC climatology (black line) as well as the equilibrium temperature profiles (gray dashed lines).

$2\,\mathrm{K\,km}^{-1}$ lies in between: Its temperature in the UTLS is higher than the equilibrium temperature, but less so than for $\gamma = 1\,\mathrm{K\,km}^{-1}$. The non-linear behavior of the deviation from the equilibrium temperature is illustrated for a variety of values of γ and p_{Tw} in Fig. 12: in the lower stratosphere, $T - T_{\mathrm{equ}}$ is larger for lower values of γ. However, the response to lowering p_{Tw} reverses from low to high values of γ. In the upper stratosphere, the deviation in temperature increases nearly linearly, both for

5   enhancing γ and p_{Tw}. At the same time, the strength of the polar vortex increases, as expected from the stronger meridional temperature gradient induced by larger γ and p_{Tw} (see Fig. 11, here the polar vortex is measured by the zonal mean wind speed at $60°\mathrm{N}$ and $10\,\mathrm{hPa}$), but this increase is again not linear in γ. The modified strength of the polar vortex is also reflected in changes in its variability, as shown in Fig. 5 for the simulations with $p_{\mathrm{Tw}} = 400\,\mathrm{hPa}$ and $\gamma = 1$, 2, and $3\,\mathrm{K\,km}^{-1}$. While the simulation with the weakest polar vortex ($\gamma = 1\,\mathrm{K\,km}^{-1}$) exhibits large variability with frequent crossings of the zero-wind

10   line (indicative of sudden stratospheric warmings), in the simulation with $\gamma = 3\,\mathrm{K\,km}^{-1}$ the wind oscillates around its large mean value without crossing the zero wind line. In the simulation with $\gamma = 2\,\mathrm{K\,km}^{-1}$, episodes with strong stable winds are disrupted by sudden decelerations, and the polar vortex remains in a weak state for up to 500 days thereafter. This behavior indicates that the vortex alternates between a strong and a weak regime.

Overall, the stratospheric circulation responds non-linearly to modifications of the winter equilibrium temperature profile.

15   Lowering the height at which the equilibrium temperature starts to decrease can diminish the high-latitude lower stratospheric temperature bias. To more or less completely remove the warm bias and the associated unrealistic "step", p_{Tw} has to be lowered to $400\,\mathrm{hPa}$. In the simulation set-up with $p_{\mathrm{Tw}} = 400\,\mathrm{hPa}$ and $\gamma = 2\,\mathrm{K\,km}^{-1}$, the winter high-latitude temperature profile is close to reanalysis data (SPARC climatology and ERA-Interim, the latter not shown) in the UTLS region and a moderate oscillation of the temperature in the upper atmosphere is simulated. The corresponding climatologies of zonal mean

20   temperature and zonal mean zonal wind of this simulation are displayed in the left panel of Fig. 10. As discussed above,

the polar vortex transitions from a weak state to a strong state when increasing γ and/or p_{Tw}. In between, vortex states are found that appear to alternate between those two states, indicative of a regime-like behavior. The dynamical reasons for this regime-like behavior will be investigated in future studies.

4.3 Planetary wave generation with topography versus heating

5 In the experiments presented in the preceding subsection 4.2, an idealized topography was used to generate planetary waves. Recently, Lindgren et al. (2018) suggested an alternative method to generate planetary waves: they introduced a tropospheric wave-like thermal forcing of the form of Eq. (12), which is added to the temperature tendency (Eq. (1)) of Newtonian cooling.

For the equilibrium temperature, Lindgren et al. (2018) employ a constant transition pressure of $p_{\mathrm{T}}(\phi) = 200\,\mathrm{hPa}$, i.e. $p_{\mathrm{Ts}} = p_{\mathrm{Tw}} = 200\,\mathrm{hPa}$, and $\epsilon = 0$, i.e., a hemispherically symmetric temperature distribution in the troposphere. Fig. 9 shows

10 the temperature profiles in the winter high latitudes for different simulations that were thermally forced by Eq. (12). The model simulation with the original Lindgren set-up exhibits a too high temperature in the winter high-latitude UTLS region compared to the SPARC climatology for the same reason as was explained for the topographically forced simulations with $p_{\mathrm{T}}(\phi) = 100\,\mathrm{hPa}$ (original PK02 set-up) in the previous subsection: the decrease of the equilibrium temperature due to γ starts too high to be able to compensate the warm bias. This motivated the investigation of model simulations with a larger transition

15 pressure p_{Tw} in the winter high latitudes for the thermally forced simulations as well.

In our model simulations with WN2 tropospheric heating, we similarly use $\epsilon = 0$, but return to $p_{\mathrm{Ts}} = 100\,\mathrm{hPa}$ and vary p_{Tw}.[1] In addition to the profile obtained from the Lindgren set-up, Fig. 9 contains the winter high-latitude temperature profiles for different polar vortex lapse rates, γ, for $p_{\mathrm{Tw}} = 400\,\mathrm{hPa}$ (left panel) and $p_{\mathrm{Tw}} = 450\,\mathrm{hPa}$ (right panel). Besides the SPARC temperature profile for January conditions, both panels show the reference model simulation for WN2 topography (with $\gamma =$

20 $2\,\mathrm{K\,km^{-1}}$ and $p_{\mathrm{Tw}} = 400\,\mathrm{hPa}$, labeled EMIL_400_2). For $p_{\mathrm{Tw}} = 400\,\mathrm{hPa}$, two circulation regimes are found. One regime is found in the model runs with $\gamma = 1\text{--}3\,\mathrm{K\,km^{-1}}$, manifesting in a positive temperature bias in the UTLS region of the winter high latitudes, with enhanced temperature compared to the equilibrium temperature (see Fig. 12 bottom right) and a weak polar vortex (see Fig. 11 bottom right). The other regime arises for $\gamma \geq 3.5\,\mathrm{K\,km^{-1}}$, with temperature following the equilibrium temperature very closely in the UTLS region (see Fig. 12 bottom right) with a strong polar vortex (see Fig. 11 bottom right).

25 For $p_{\mathrm{Tw}} = 450\,\mathrm{hPa}$, these two regimes exist for $\gamma = 1\text{--}2.5\,\mathrm{K\,km^{-1}}$ and $\gamma \geq 3.5\,\mathrm{K\,km^{-1}}$, respectively (see Fig. 9 right panel). However, the resulting circulation for $\gamma = 3\,\mathrm{K\,km^{-1}}$ can not be assigned to one of the regimes, since the temperature in the UTLS region is neither too warm nor follows its equilibrium temperature, i.e., with a similar behavior as the topographically-forced simulation with $p_{\mathrm{Tw}} = 400\,\mathrm{hPa}$ and $\gamma \geq 2\,\mathrm{K\,km^{-1}}$. The climatologies of those two simulations are shown in Fig. 10.

The response of the polar vortex to changes in the equilibrium temperature is similar between the topographically versus

30 thermally forced model simulations in that a regime shift from a weak to a strong polar vortex is found for both cases. However, other aspects of the circulation response show distinct differences. The response of the residual meridional circulation is exam-

---

[1] The difference in the equilibrium temperature between $p_{\mathrm{Ts}} = 100\,\mathrm{hPa}$ and $p_{\mathrm{Ts}} = 200\,\mathrm{hPa}$ is marginal since the US standard atmosphere between $\sim 55\,\mathrm{hPa}$ and $\sim 226\,\mathrm{hPa}$ is isothermal at $216.65\,\mathrm{K}$. Thus, for different values of p_{Tw} only the lower region of the polar vortex lapse rate around $\phi_0 = 50°\mathrm{N}$ experiences a slight change when employing $p_{\mathrm{Ts}} = 100\,\mathrm{hPa}$ instead of $p_{\mathrm{Ts}} = 200\,\mathrm{hPa}$.
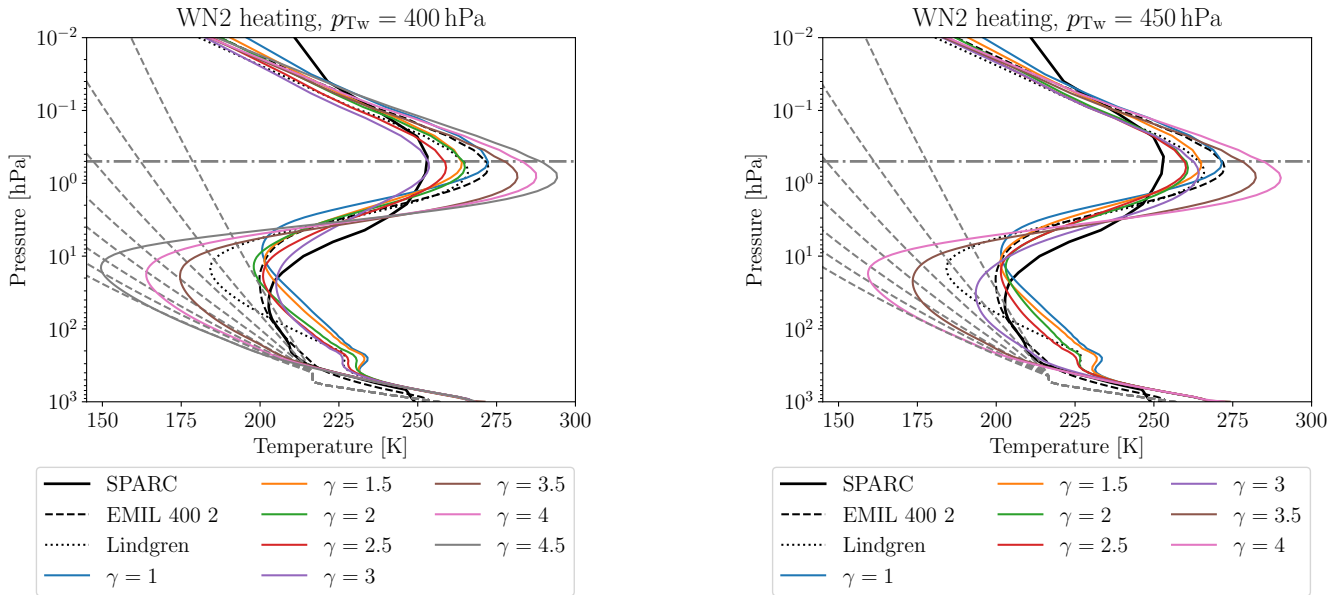
Figure 9. Same as Fig. 8, but for model simulations with WN2 tropospheric heating of amplitude $q_0 = 6\,\mathrm{K\,day}^{-1}$ and different polar vortex lapse rates γ for $p_{\mathrm{Tw}} = 400\,\mathrm{hPa}$ (left) and $p_{\mathrm{Tw}} = 450\,\mathrm{hPa}$ (right). The temperature profiles obtained from a simulation with WN2 topography, $\gamma = 2\,\mathrm{K\,km}^{-1}$ and $p_{\mathrm{Tw}} = 400\,\mathrm{hPa}$ (black dashed line) and from the Lindgren set-up (black dotted line) are added for comparison.
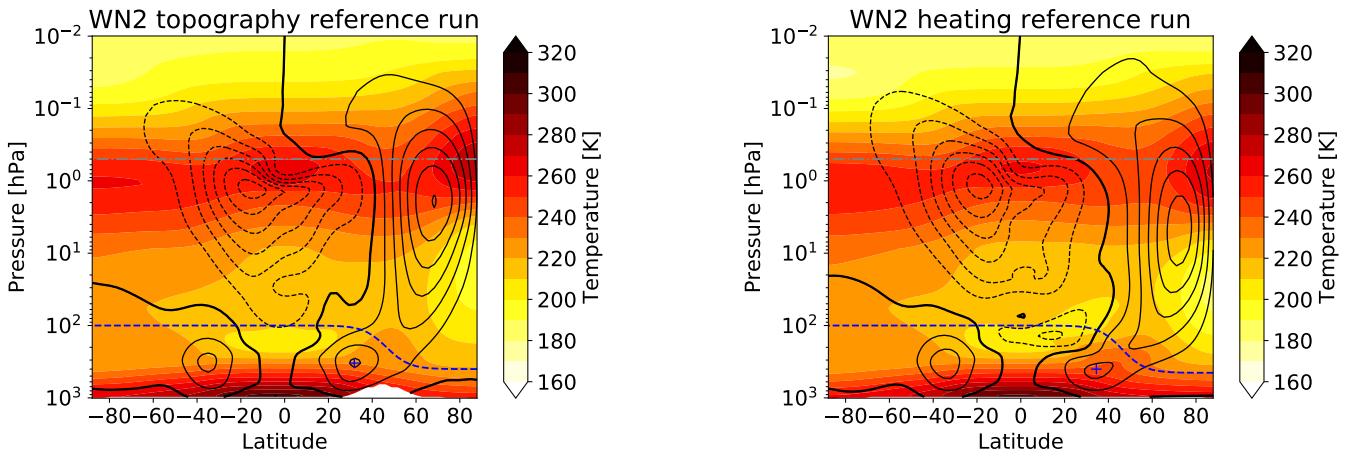
Figure 10. Temperature [K] and zonal wind [ms^{-1}] climatologies of model simulations with idealized topography of height $h = 3\,\mathrm{km}$ (left panel) and the simulations with idealized tropospheric heating of amplitude $q_0 = 6\,\mathrm{K\,day}^{-1}$ (right panel). The winter high latitude transition pressures and polar vortex lapse rates are $p_{\mathrm{Tw}} = 400\,\mathrm{hPa}$ and $\gamma = 2\,\mathrm{K\,km}^{-1}$ for the topographically forced model simulation and $p_{\mathrm{Tw}} = 450\,\mathrm{hPa}$ and $\gamma = 3\,\mathrm{K\,km}^{-1}$ for the thermally forced model simulation, respectively.

ined in terms of the difference of temperature and equilibrium temperature, a valid measure of the strength of this circulation in the idealized model (see e.g., Jucker et al., 2013). We choose to average this temperature difference from $40°\text{N}$ to $90°\text{N}$ to have a positive quantity due to the diabatic heating in that region. Larger values of this temperature difference therefore imply a stronger circulation. In Fig. 12, these temperature differences are displayed for $1\,\text{hPa}$ and $100\,\text{hPa}$ to represent the strength

5 of the circulation in the lower and upper stratosphere, respectively. Again, in case of a topographically forced circulation, the result of Gerber (2012) is reproduced, according to which a stronger polar vortex leads to a strengthened circulation in the upper stratosphere and to a weakened circulation in the lower stratosphere (see Fig. 3 of Gerber, 2012, for comparison) . Thermally forced model simulations show the same increase of the strength of the meridional circulation at $1\,\text{hPa}$, although the polar vortex increases in strength only for larger γ. However, at $100\,\text{hPa}$, a nonlinear behavior in the strength of the meridional

10 circulation is observed. For low values of the polar vortex lapse rate γ, the circulation strengthens, but for higher values, the circulation weakens as expected from the topographically forced model simulations. The change in the behavior of the meridional circulation in the model simulations with $p_{\text{Tw}} = 400\,\text{hPa}$ and $p_{\text{Tw}} = 450\,\text{hPa}$ appears at the same polar vortex lapse rates, at which the polar vortex starts to strengthen.

Further, we compare the response of the tropospheric jet to changed equilibrium temperatures in topographically forced

15 simulations to the response in the thermally forced simulations. In Fig. 11, next to the strength of the polar vortex, the latitude of the zonal mean zonal wind speed maximum of the tropospheric jet for varying polar lapse rates γ and transition pressures p_{Tw} are shown. Both, for the topographically and thermally forced simulations, the polar vortex strength generally increases with larger polar lapse rate γ and a transition pressure at lower heights (higher p_{Tw}), as expected. However, the increase is not linear, in particular in the thermally forced simulations, where the polar vortex increases in strength only for $\gamma > 3\,\text{K}\,\text{km}^{-1}$.

20 In case of the topographically forced model simulations (upper panels), the result of Gerber and Polvani (2009) is reproduced according to which a stronger stratospheric polar vortex causes a northward shift of the tropospheric jet stream (see their Fig. 2 for comparison). However, when the circulation is thermally forced, this behavior is not observed (see lower panels of Fig. 11). Even strong increases in the stratospheric polar vortex for $\gamma > 3\,\text{K}\,\text{km}^{-1}$ at $p_{\text{Tw}} = 400\,\text{hPa}$ and for $\gamma > 2.5\,\text{K}\,\text{km}^{-1}$ at $p_{\text{Tw}} = 450\,\text{hPa}$, respectively, are not accompanied by a northward shift of the tropospheric jet maximum. On the contrary, a

25 slight southward shift is observed.

The different behavior of model simulations with topographically and thermally forced circulations outlined here indicates that the thermally forced simulations will have to be used with caution, in particular for studying troposphere-stratosphere coupling.

5 Application examples

30 In the following, two examples of research applications with the dynamical core model are shown. First, variability and changes in tracer transport in response to changes in the polar vortex are analyzed, using the simulation set-up with the modified equilibrium temperature (see Sec. 4.2). Secondly, the localized heating routine (see Sec. 2.1.3) is used to force an idealized monsoon circulation system.
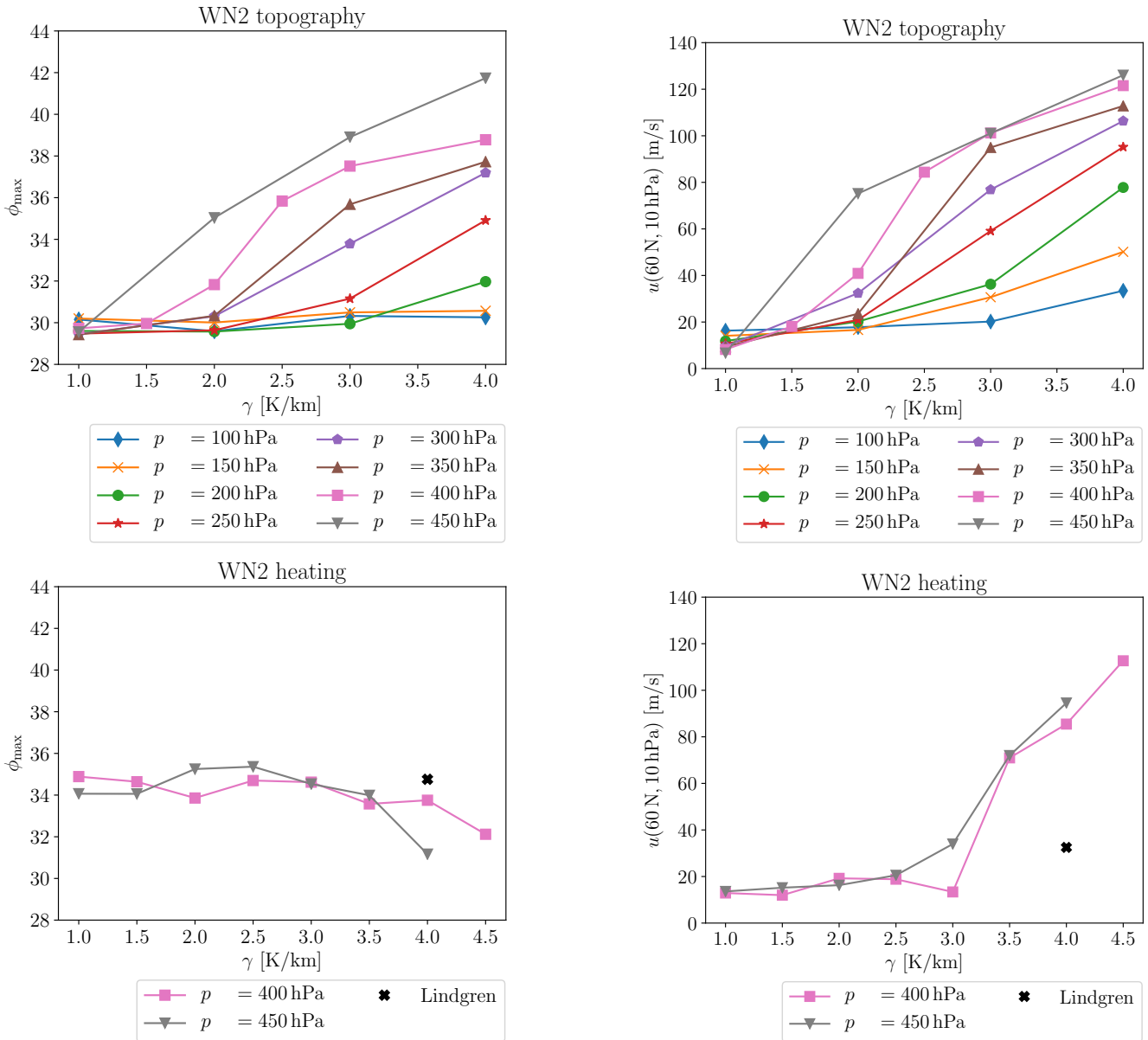
Figure 11. Latitude ϕ_{max} of the zonal mean zonal wind speed maximum of the tropospheric subtropical jet stream (left panels) and zonal mean zonal wind speed u at $60°\mathrm{N}$ and $10\,\mathrm{hPa}$ (right panels) for model simulations with WN2 topography of height $h = 3\,\mathrm{km}$ (upper panels) and WN2 tropospheric heating of amplitude $q_0 = 6\,\mathrm{K}\,\mathrm{day}^{-1}$ (lower panels).
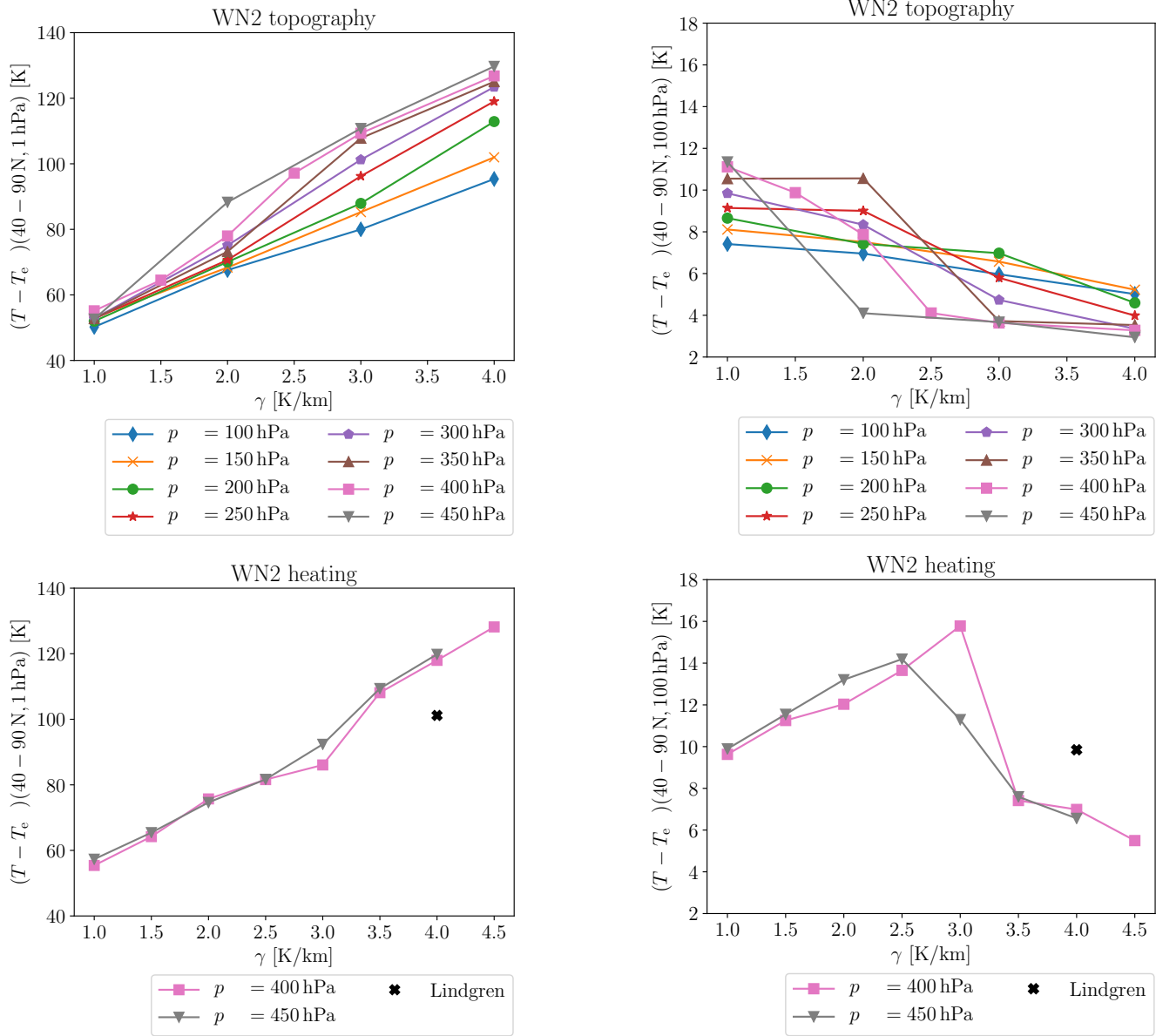
Figure 12. Difference of temperature and equilibrium temperature $T - T_{\mathrm{equ}}$ averaged from $40°\mathrm{N}$ to $90°\mathrm{N}$ at $1\,\mathrm{hPa}$ (left panels) and $100\,\mathrm{hPa}$ (right panels) for model simulations with WN2 topography of height $h = 3\,\mathrm{km}$ (upper panels) and WN2 tropospheric heating of amplitude $q_0 = 6\,\mathrm{K}\,\mathrm{day}^{-1}$ (lower panels).

5.1 Chemistry and tracer transport

With the implementation of the idealized model set-up in the MESSy framework, all tracer utility and chemistry submodels can be easily used to study the tracer transport in the idealized model. Within the chemistry submodel MECCA (Sander et al.,

2019), tailor made chemical mechanisms can be selected to the users' needs, allowing for the set-up of simplified chemistry. As a proof of concept, we present results from simulations where the only selected chemical reactions are the photolysis of Chlorofluorocarbons (CFCs, namely CFC-11 and CFC-12).

Technically, this simulation set-up requires, in addition to the "standard" EMIL set-up, to switch on submodels for solving
5 chemical kinetics (MECCA, Sander et al., 2019), for calculating photolysis rates (JVAL, Sander et al., 2014), for determining orbital parameters (ORBIT, Dietmüller et al., 2016) and submodels for tracer definition (TRACER and PTRAC, Jöckel et al., 2008) and tracer boundary condition nudging (TNUDGE, Kerkweg et al., 2006). CFC mixing ratios were set to values representative of year 2000 at the surface, and tracers were initialized with a mean distribution from an earlier EMAC simulation. To obtain constant January conditions of solar irradiance (compatible with the idealized thermodynamical forcing of the
10 dynamics), in the "TIMER" namelist, a perpetual month simulation can be selected.

With the given model set-up including chemical tracers, the influence of idealized dynamical variability on chemically active species can be studied. Shown in Fig. 13 are zonal mean CFC-11 mixing ratios at 50 hPa as function of latitude and time in a simulation with PK set-up with p_{Tw}=400 hPa and γ=2 K km^{-1}. The polar vortex variability leads to variability in CFC-11 mixing ratios in particular at high latitudes. As diagnosed from the time series of zonal wind at 60°N and 10 hPa (top panel
15 in Fig. 13, black line) sudden stratospheric warming (SSW) events occur at around day 600 and day 1350 (defined as zero-crossing of the zonal wind), both followed by an extended period with a weak polar vortex. For both events, the CFC-11 mixing ratios drop at high latitudes simultaneously with the drop of zonal winds at 10 hPa. However, around 200 days after the SSW events, mixing ratios are anomalously high. This behavior can be explained as follows: simultaneously with the SSW, strong downwelling occurs at high latitudes (north of 60°N, and driven by the strong wave dissipation that causes SSWs, see
20 red line in top panel in Fig. 13), thus transporting CFC-depleted air from higher altitudes downward. However, due to the diminished vortex in the period after the SSW, air from mid-latitudes with higher CFC mixing ratios can be mixed towards the pole, thus leading to an enhancement of CFC mixing ratios at high latitudes (evident in Fig. 13 around days 800-1000 and days 1500-1700, when zonal winds are below 15 ms^{-1}). Those transport anomalies are evident in the latitudinal profiles of CFC-11 mixing ratios, as shown in the right panel of Fig. 13: during episodes with a strong polar vortex (solid line), there is
25 a minimum in mixing ratios close to the polar vortex edge (in agreement with strongest downwelling at the vortex edge, see Fig. 14, third panel), denoting the separation between mid-latitude and high-latitude air by the vortex. Just at and after the SSW events, CFC mixing ratios drop at high latitudes (dashed line), while in the episodes with eroded vortex, CFC-11 mixing ratios are enhanced at high latitude and no mixing barrier can be identified (dotted line). As demonstrated here, the idealized set-up of the simulation allows to study the role of vortex variability on tracer mixing ratios in an isolated manner.

30 Two additional simulations were performed with idealized changes in the polar vortex (intermediate: $\gamma = 2$, weak vortex: $\gamma = 1$, strong vortex $\gamma = 3$). The resulting climatological mean CFC-11 mixing ratios at 50 hPa are shown in Fig. 14 (top). The differing dynamical states of the three simulations are clearly reflected in the tracer mixing ratios: The simulation with the weak vortex ($\gamma = 1$, red) shows highest CFC-11 mixing ratios in the tropics to mid-latitudes, with a smooth transition from tropics to high-latitudes, in line with strongest upwelling (see Fig. 14c; see also results in Sec. 4.2) and strong mid-latitudes wave driving
35 that results in mixing (see Fig. 14d). In the simulation with a strong vortex ($\gamma = 3$, blue), mixing ratios in the tropics are weaker,
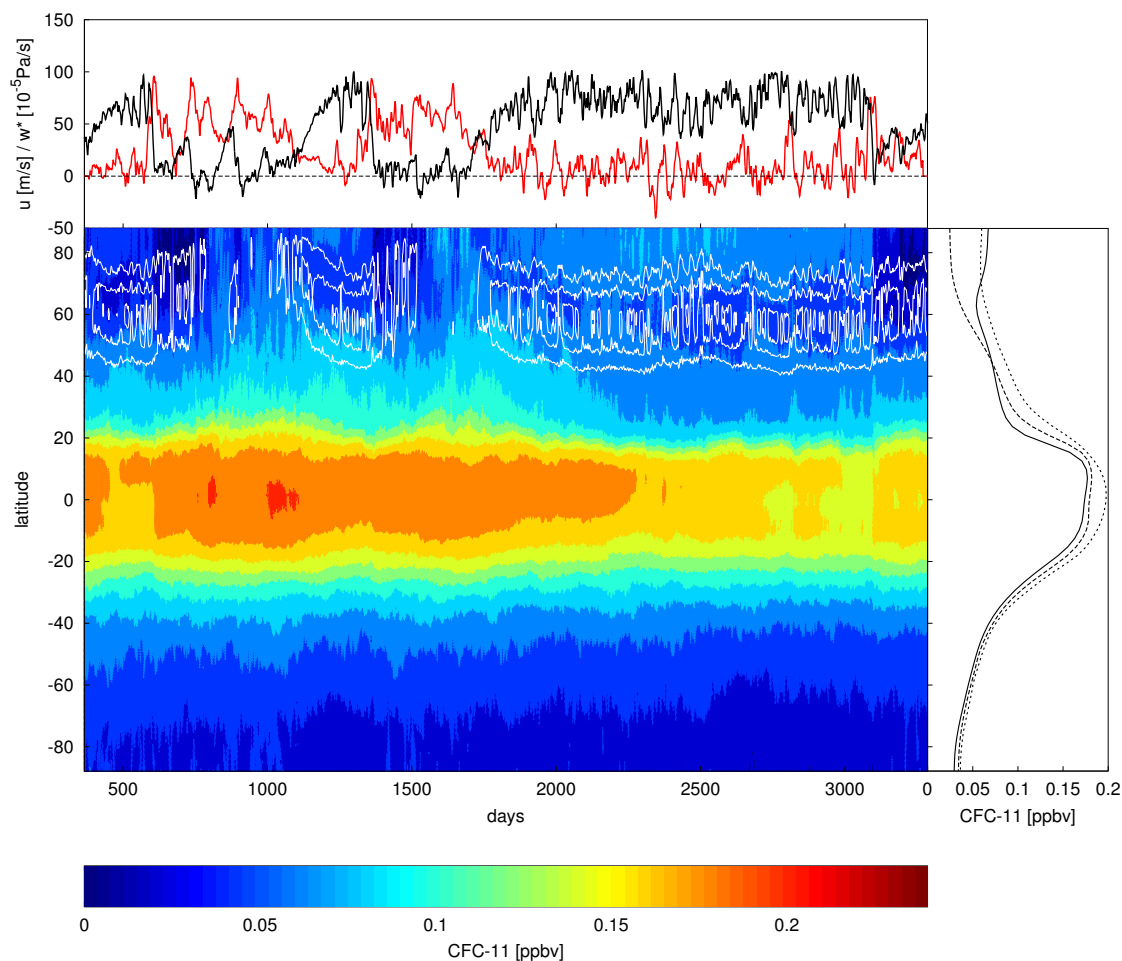
Figure 13. Zonal mean CFC-11 mixing ratios [ppbv] at 50 hPa as function of simulated day and latitude (color), and zonal mean zonal wind (white contours, interval $15\,\mathrm{ms^{-1}}$). Top: time series of zonal mean zonal wind at 60N and 10hPa (black) and mean $\overline{w^*}$ at 50 hPa and 60-90N (red, in 10^{-5}Pa/s). Right: time-mean CFC-11 mixing ratios as function of latitude over days with strong vortex (days 400-600; 1200-1350; 2000-3000, black solid), over days following SSW with strong downwelling (day 600-780; 1380-1500; 3100-3280, dashed) and over days with eroded polar vortex (day 800-1000 and 1580-1700, dotted).

due to weaker upwelling in the lower stratosphere (see also Fig. 12), and the gradient to mid-latitudes is steep. This can be explained both due to weaker mixing (see Fig. 14d) as well as stronger downwelling within the mid-latitudes (see Fig. 14c). Indeed, downwelling maximizes at the equatorward flank of the polar vortex (both in the $\gamma = 3$ and 2 simulations), and is weak within the vortex, in contrast to the $\gamma = 1$ simulation, where downwelling maximizes more poleward and is stronger also at

5 high latitudes. The maximum of downwelling in the mid-latitudes as well as the high isolation of vortex air in the strong vortex

case likely explains why CFC-11 mixing ratios are elevated within the vortex. The intermediate simulation with $\gamma = 2$ lies in between the other two simulations, but shows highest variability (largest standard deviation) in most quantities, as expected, since this simulation transitions between states with weak and strong vortex (see Fig. 13 and Sec.4.2).

5.2 Monsoon anticyclone forced by localized idealized heating

5 Understanding the monsoon systems is a key task (Turner and Annamalai, 2012) and idealized models have been widely used to understand the basic processes occuring in the monsoon regions (e.g., Gill, 1980; Yano and L. McBride, 1998; Bordoni and Schneider, 2008). In particular, also the development and dynamics of the monsoon anticyclones over Asia (e.g., Gill, 1980; Hoskins and Rodwell, 1995; Liu et al., 2007; Wei et al., 2014, 2015; Hsu and Plumb, 2000; Amemiya and Sato, 2018) and North America (Siu and Bowman, 2019) have been investigated using simplified modelling approaches. Here we impose an idealized

10 heating field to divert the circulation from the basic state. In the following we show results from a T42L90MA simulation with the *'HS'* set-up of equilibrium temperature and NH summer constellation, i.e., hemispheric asymmetry is caused by setting the asymmetry factor ϵ to 10. On top of the basic state a regionally confined heating source is imposed in the NH tropics to subtropics (following Eqs. 13-17 with $\phi_0 = 20°$ N, $\lambda_0 = 90°$ E, $\delta\phi = 10°$, $\delta\lambda = 30°$). Vertically the heating extends from $p_{bot} = 800\,\mathrm{hPa}$ to $p_{top} = 100\,\mathrm{hPa}$. The heating is turned on at day 0 of the simulation with a spin up of $t_s = 20\,\mathrm{days}$. Other

15 temporal variations are not considered as $q_{temp} = 0\,\mathrm{K\,day^{-1}}$. The temporally constant (neglecting the spin-up period) heating is imposed with $q_0 = 8\,\mathrm{K\,day^{-1}}$. After the spin-up period, the average total energy per day that is added into the model due to this additional heat source (deduced from 6 h model output) is slightly below 21×10^{19} J.

The mean geopotential height field for this T42L90MA simulation with the described idealized heating is shown in Fig. 15. A clear anticyclone is produced from the additional heating. This anticyclone is similar to the Asian monsoon anticyclone

20 (e.g., Hoskins and Rodwell, 1995; Zhang et al., 2002; Randel and Park, 2006; Nützel et al., 2016). Fig. 15 shows a latitude vs. pressure cross section of zonal winds averaged over all longitudes. The zonal winds averaged over the anticyclone region are overlayed in black contours. The positive wind speed in the north and the negative wind speeds towards the equator marking the edges of the anticyclone are clearly visible (cf. Figs. 2 and 1 in Randel and Park, 2006; Garny and Randel, 2016, respectively). Fig. 16 shows the temporal variation of the anticyclone during two periods of the simulation. On the left of Figure 16, an

25 example of a splitting event of the anticyclone is shown. On the first day of the depicted period, the anticyclone is elongated. After that the anticyclone splits and two and four days later two anticyclone centers can be identified. Six days after the elongated phase, the western center has decayed and the eastern center has moved back westwards to roughly $90°$ E. Such splitting events (sometimes also denoted westward eddy sheddings, Figs. 15 and 16 in Hsu and Plumb, 2000), as shown in Fig. 16 are (typical) features during the monsoon period in observations (e.g., Fig. 13 in Garny and Randel, 2013; Vogel et al.,

30 2015; Nützel et al., 2016; Pan et al., 2016). Also eastward eddy shedding as found during the second period as displayed on the right of Fig. 16 has been previously noted in a couple of publications (e.g., Dethof et al., 1999; Garny and Randel, 2013; Vogel et al., 2014; Nützel et al., 2016) and consitutes a major mode of variability observed in the monsoon anticyclone. During the depicted period on the eastern edge of the anticyclone a filament is torn off. On the first day the anticyclone is nearly

unperturbed, while two days later the anticyclone extends clearly to the west and again two days later a filament is separated from the main anticyclone.

Those examples show that by imposing an idealized monsoon-like heating in the dynamical core model, the monsoon anticyclone can be simulated with realistic mean state and variability. The variability of the anticyclone under constant versus
5 time-varying forcing, and its impact on troposphere-stratosphere tracer transport will be the subject of future studies.

6   Summary and Outlook

In the paper presented here, the implementation of a dry dynamical core model set-up within the ECHAM/MESSy model system, the ECHAM/MESSy IdeaLized (EMIL) model set-up is documented. It is shown that earlier dry dynamical core model simulation with ECHAM5 and other models are closely reproduced by EMIL simulations with same set-ups.

10   The implementation of the submodel RELAX, necessary for the dynamical core set-up, includes pre-implemented functions for the parameters for Newtonian cooling and Rayleigh friction based on the suggestions by HS94 and PK02, but with extensions, and further the option to set the parameters to arbitrarily defined fields, which are read from external files. Further, it includes the possibility to include additional diabatic heating either by pre-implemented functions for zonal mean, localized or wave-like heating, or by externally read files. Thus, the implementation provides a tool-kit for the users to chose model set-ups
15 to their needs.

Modifications to the set-up by PK02 and Gerber and Polvani (2009), which were used frequently in the past, are presented with respect to the shape of the upper sponge layer and with respect to the equilibrium temperature profile in the winter stratosphere. The damping coefficient of the upper sponge layer is set to increase exponentially with height instead of quadratically, resembling more closely parametrized drag by GW in the full model and leading to more realistic temperature profiles in the
20 stratopause region. However, the impact outside the sponge layer is limited to above 10 hPa and to high latitudes. Modifications of the equilibrium temperature in the high latitude UTLS region are performed by increasing the transition pressure (p_{Tw}) between troposphere and stratosphere at high-latitudes (thus, the decrease of temperatures forming the polar vortex starts at lower altitudes). We find that increasing the transition pressure from 100 hPa to 400 hPa results in a realistic mean temperature profile (with the polar lapse rate $\gamma = 2$), thus correcting for the UTLS warm bias of the PK02/ Gerber and Polvani (2009) simulations.
25 The increased transition pressure causes climate states, in which a regime-like behavior becomes more pronounced than in the previously used set-ups: the polar vortex appears to transition from a weak to a strong regime, and the simulation with the most realistic mean temperature profile is at the transition point between those regimes.

Simulations with planetary wave generation by topography and by wave-like heating (as suggested by Lindgren et al., 2018) are contrasted. Generally, similar basic states can be simulated with the two different set-ups, and in both cases increases in γ
30 lead to increases in the polar vortex strength and mid-stratospheric downwelling. However, the heating-forced simulations react more non-linear to increases in γ both in terms of polar vortex strength and lower stratospheric downwelling. Furthermore, while in the topographically forced simulations the tropospheric jet moves poleward with a stronger polar vortex (in agreement with Gerber and Polvani, 2009), the tropospheric jet remains at a fixed latitude in the simulations with wave-like heating. These

results indicate that the wave-like heating does not allow for stratospheric influences on the tropospheric jet. Further work will be necessary to understand this behavior. Overall, we recommend to use the thermally forced wave generation with caution.

As a first application example of the dry dynamical core model we present as a proof-of-concept a simulation with very basic chemistry (here only photolysis of CFCs), and the potential of such simulation set-ups to study the impact of dynamical 5 variability and changes on tracer transport in an idealized fashion is shown. The set of chemical reactions can be expanded to the user's needs to study transport of more complex chemical tracers, such as ozone.

Secondly, we present a simulation of a monsoon-like upper tropospheric anticyclonic circulation with realistic variability forced by imposed localized heating. Such a set-up can be used to study the dynamics of diabatically forced circulation systems such as monsoon anticyclones under different forcings and background states.

10 With the dry dynamical core model set-up, the model hierarchy within the ECHAM/MESSy model system is extended by a commonly used model set-up for studying dynamical and transport processes, including the possibility to consider chemically active tracers. As a next step, we envision an expansion to account for chemistry-dynamics interaction in a simplified manner as an intermediate step between the dry dynamical core model and the full CCM.
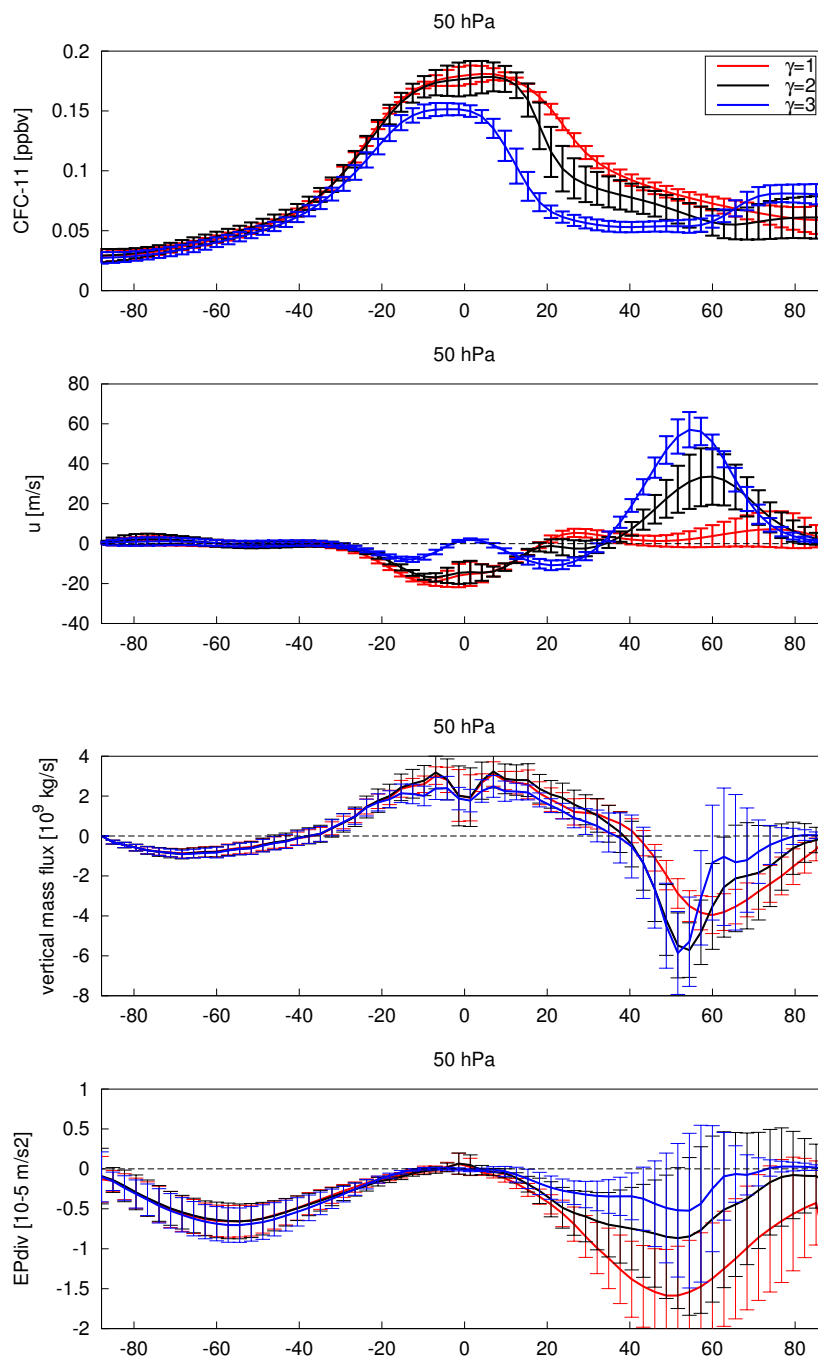
Figure 14. a) Zonal mean CFC-11 mixing ratios at 50 hPa as function of latitude for EMIL simulations with *PK* set-up with p_{Tw}=400 hPa and $\gamma = 1$ (red) , 2 (black) and 3 (blue), b) zonal mean zonal wind , c) mean vertical mass flux and d) EP flux divergence.
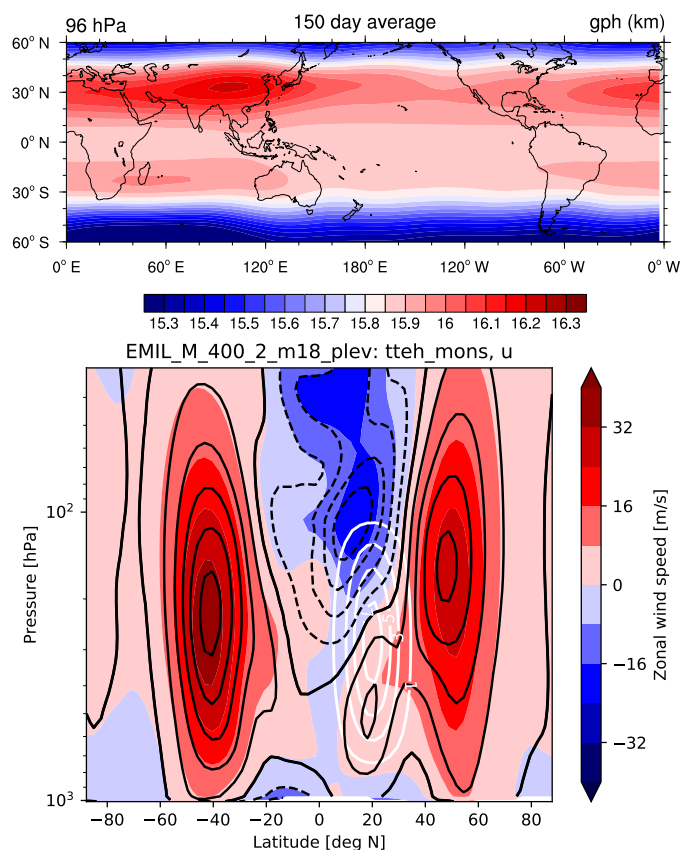
Figure 15. Top: Mean anticyclone structure via geopotential height (km) at ~100 hPa from 150 days of the integration (map included for orientation and scale purposes only; i.e., the simulation features no orography etc.). Bottom: Vertical cross section of zonal mean wind (colour-coded) and wind in the anticyclone region (averaged over 60-120°E; black contours). White contours show the maximum along the longitudes of the implied heating function (in K/day).
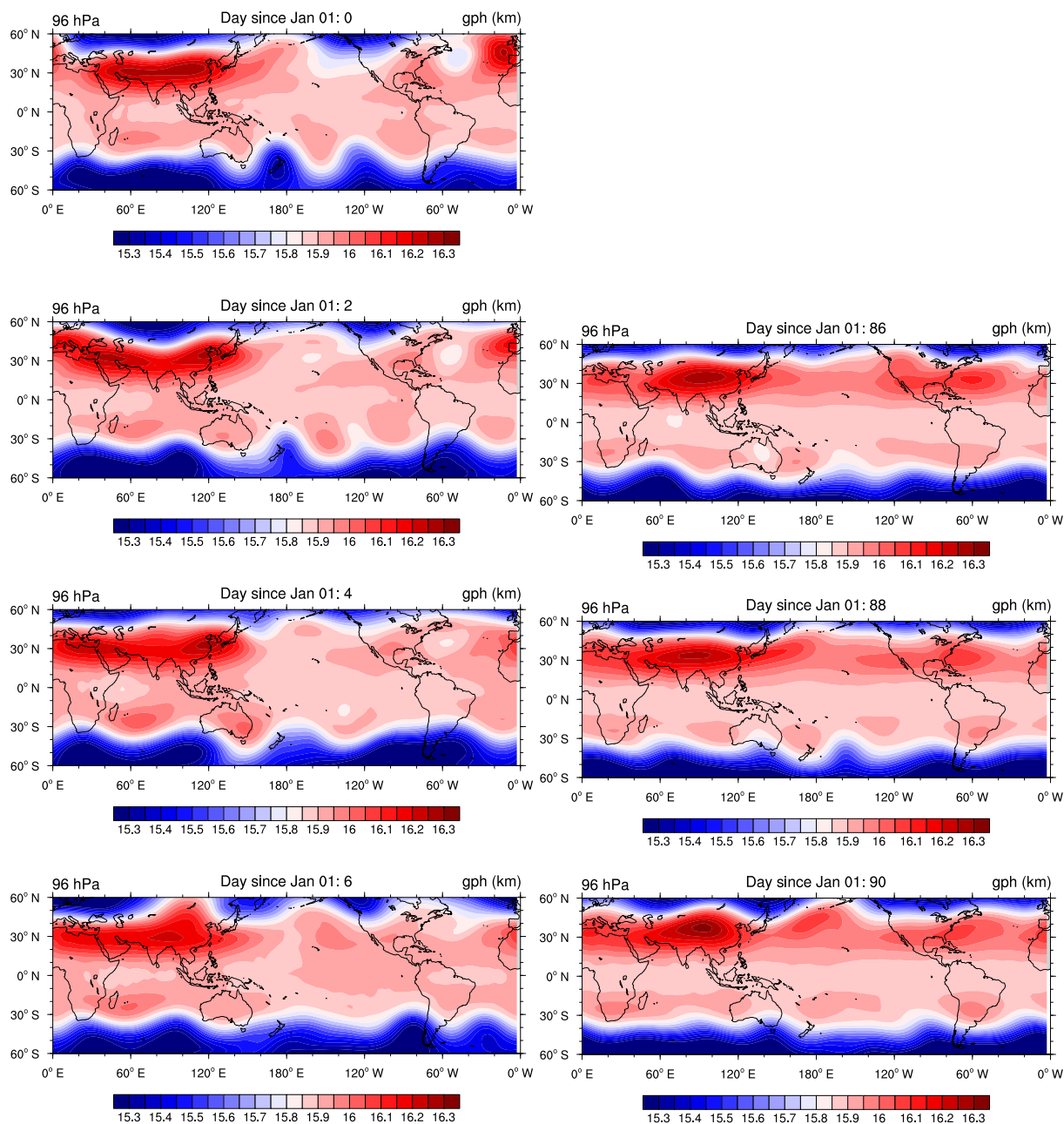
Figure 16. Evolution of geopotential height at ∼100 hPa showing an example of a splitting event (left, over the period of 7 days), and an eastward shedding event (right, over a 5 day period).

Code availability. The Modular Earth Submodel System (MESSy) is continuously further developed and applied by a consortium of insti-

15 tutions. The usage of MESSy and access to the source code is licenced to all affiliates of institutions which are members of the MESSy Consortium. Institutions can become a member of the MESSy Consortium by signing the MESSy Memorandum of Understanding. More information can be found on the MESSy Consortium Website (http://www.messy-interface.org). The code presented here has been based on MESSy version 2.54 and will be available in the next official release (version 2.55).

Author contributions. HG designed and performed the implementation of the submodel RELAX, performed the test simulations and wrote

20 large parts of the paper. RW strongly contributed to the implementation and conducted, analyzed and described the sensitivity experiments. MN implemented the localized heating function and analyzed and described the monsoon experiments. All authors contributed to the writing of the paper.

Competing interests. The authors hereby declare that they do not have conflicting interests.

Acknowledgements. HG and RW were funded by the Helmholtz Association under grant VH-NG-1014 (Helmholtz-Hochschul- Nachwuchs-

25 forschergruppe MACCClim). MN received funding from the Initiative and Networking Fund of the Helmholtz Association through the project "Advanced Earth System Modelling Capacity (ESM). The simulations have been performed at the German Climate Computing Centre DKRZ through support from the Bundesministerium für Bildung und Forschung (BMBF). Data was processed using CDO (Climate Data Operators; Schulzweida, 2019). For parts of the data analysis and plotting NCL (NCAR Command Language; NCL, 2018) has been used. We thank Patrick Jöckel for useful discussion and comments, and Philip Rupp for helpful discussions on idealized modelling of monsoon anticyclones.

References

NCL: The NCAR Command Language (Version 6.5.0) [Software], Boulder, Colorado, UCAR/NCAR/CISL/TDD, 2018.

Amemiya, A. and Sato, K.: A Two-Dimensional Dynamical Model for the Subseasonal Variability of the Asian Monsoon Anticyclone, Journal of the Atmospheric Sciences, 75, 3597–3612, https://doi.org/10.1175/JAS-D-17-0208.1, 2018.

Bordoni, S. and Schneider, T.: Monsoons as eddy-mediated regime transitions of the tropical overturning circulation, Nature Geosci, 1, 515–519, http://dx.doi.org/10.1038/ngeo248, 2008.

Butler, A. H., Thompson, D. W. J., and Heikes, R.: The Steady-State Atmospheric Circulation Response to Climate Change-like Thermal Forcings in a Simple General Circulation Model, Journal of Climate, 23, 3474–3496, https://doi.org/10.1175/2010JCLI3228.1, 2010.

Chen, G., Held, I. M., and Robinson, W. A.: Sensitivity of the Latitude of the Surface Westerlies to Surface Friction, Journal of Atmospheric Sciences, 64, 2899, 2007.

Deckert, R., Jöckel, P., Grewe, V., Gottschaldt, K.-D., and Hoor, P.: A quasi chemistry-transport model mode for EMAC, Geoscientific Model Development, 4, 195–206, https://www.geosci-model-dev.net/4/195/2011/, 2011.

Dee, D. P., Uppala, S. M., Simmons, A. J., Berrisford, P., Poli, P., Kobayashi, S., Andrae, U., Balmaseda, M. A., Balsamo, G., Bauer, P., Bechtold, P., Beljaars, A. C. M., van de Berg, L., Bidlot, J., Bormann, N., Delsol, C., Dragani, R., Fuentes, M., Geer, A. J., Haimberger, L., Healy, S. B., Hersbach, H., Holm, E. V., Isaksen, L., Kållberg, P., Köhler, M., Matricardi, M., McNally, A. P., Monge-Sanz, B. M., Morcrette, J.-J., Park, B.-K., Peubey, C., de Rosnay, P., Tavolato, C., Thepaut, J.-N., and Vitart, F.: The ERA-Interim reanalysis: configuration and performance of the data assimilation system, Q J Roy. Meteorol. Soc., 137, 553–597, 2011.

Dethof, A., O'Neill, A., Slingo, J. M., and Smit, H. G. J.: A mechanism for moistening the lower stratosphere involving the Asian summer monsoon, Q. J. R. Meteorol. Soc., 125, 1079–1106, 1999.

Dietmüller, S., Ponater, M., and Sausen, R.: Interactive ozone induces a negative feedback in CO_2-driven climate change simulations, Journal of Geophysical Research: Atmospheres, 119, 1796–1805, https://agupubs.onlinelibrary.wiley.com/doi/abs/10.1002/2013JD020575, 2014.

Dietmüller, S., Jöckel, P., Tost, H., Kunze, M., Gellhorn, C., Brinkop, S., Frömming, C., Ponater, M., Steil, B., Lauer, A., and Hendricks, J.: A new radiation infrastructure for the Modular Earth Submodel System (MESSy, based on version 2.51), Geoscientific Model Development, 9, 2209–2222, https://www.geosci-model-dev.net/9/2209/2016/, 2016.

Frierson, D. M. W., Held, I. M., and Zurita-Gotor, P.: A Gray-Radiation Aquaplanet Moist GCM. Part I: Static Stability and Eddy Scale, Journal of the Atmospheric Sciences, 63, 2548–2566, https://doi.org/10.1175/JAS3753.1, 2006.

Garny, H. and Randel, W.: Dynamical variability in the Asian monsoon anticyclone observed in potential vorticity and correlations with tracer distributions, J. Geophys. Res. Atmos., 118, 1–13, 2013.

Garny, H. and Randel, W. J.: Transport pathways from the Asian monsoon anticyclone to the stratosphere, Atmospheric Chemistry and Physics, 16, 2703–2718, http://www.atmos-chem-phys.net/16/2703/2016/, 2016.

Gerber, E. P.: Stratospheric versus Tropospheric Control of the Strength and Structure of the Brewer-Dobson Circulation, J. Atmos. Sci., 69, 2857–2877, 2012.

Gerber, E. P. and Polvani, L.: Stratosphere-Troposphere Coupling in a Relatively Simple AGCM: The Importance of Stratospheric Variability, Journal of Climate, 22, 1920–1933, 2009.

Gerber, E. P. and Vallis, G. K.: Eddy-Zonal Flow Interactions and the Persistence of the Zonal Index, J. Atmos. Sci., 64, 2007.

Gill, A. E.: Some simple solutions for heat-induced tropical circulation, Q. J. R. Meteorol. Soc., 106, 447–462, 1980.

Held, I. I. M. and Suarez, M. M. J.: A proposal for the intercomparison of the dynamical cores of atmospheric general circulation models, Bull. Amer. Meteor. Soc., pp. 1825–1830, 1994.

Held, I. M.: The Gap between Simulation and Understanding in Climate Modeling, Bulletin of the American Meteorological Society, 86, 1609–1614, https://doi.org/10.1175/BAMS-86-11-1609, 2005.

Hoskins, B. J. and Rodwell, M. J.: A Model of the Asian Summer Monsoon. Part I: The Global Scale, J. Atmos. Sci., 52, 1329–1340, http://dx.doi.org/10.1175/1520-0469(1995)052<1329:AMOTAS>2.0.CO;2, 1995.

Hsu, C. J. and Plumb, R. A.: Nonaxisymmetric Thermally Driven Circulations and Upper-Tropospheric Monsoon Dynamics, J. Atmos. Sci., 57, 1255–1276, http://dx.doi.org/10.1175/1520-0469(2000)057<1255:NTDCAU>2.0.CO;2, 2000.

Jeevanjee, N., Hassanzadeh, P., Hill, S., and Sheshadri, A.: A perspective on climate model hierarchies, Journal of Advances in Modeling Earth Systems, 9 (4), 1760–1771, 2017.

Jöckel, P., Sander, R., Kerkweg, A., Tost, H., and Lelieveld, J.: Technical Note: The Modular Earth Submodel System (MESSy) - a new approach towards Earth System Modeling, Atmospheric Chemistry and Physics, 5, 433–444, https://www.atmos-chem-phys.net/5/433/2005/, 2005.

Jöckel, P., Tost, H., Pozzer, A., Brühl, C., Buchholz, J., Ganzeveld, L., Hoor, P., Kerkweg, A., Lawrence, M. G., Sander, R., Steil, B., Stiller, G., Tanarhte, M., Taraborrelli, D., van Aardenne, J., and Lelieveld, J.: The atmospheric chemistry general circulation model ECHAM5/MESSy1: consistent simulation of ozone from the surface to the mesosphere, Atmos. Chem. Phys., 6, 5067–5104, 2006.

Jöckel, P., Kerkweg, A., Buchholz-Dietsch, J., Tost, H., Sander, R., and Pozzer, A.: Technical Note: Coupling of chemical processes with the Modular Earth Submodel System (MESSy) submodel TRACER, Atmospheric Chemistry and Physics, 8, 1677–1687, https://www.atmos-chem-phys.net/8/1677/2008/, 2008.

Jöckel, P., Kerkweg, A., Pozzer, A., Sander, R., Tost, H., Riede, H., Baumgaertner, A., Gromov, S., and Kern, B.: Development cycle 2 of the Modular Earth Submodel System (MESSy2), Geoscientific Model Development, 3, 717–752, https://www.geosci-model-dev.net/3/717/2010/, 2010.

Jöckel, P., Tost, H., Pozzer, A., Kunze, M., Kirner, O., Brenninkmeijer, C. A. M., Brinkop, S., Cai, D. S., Dyroff, C., Eckstein, J., Frank, F., Garny, H., Gottschaldt, K.-D., Graf, P., Grewe, V., Kerkweg, A., Kern, B., Matthes, S., Mertens, M., Meul, S., Neumaier, M., Nützel, M., Oberländer-Hayn, S., Ruhnke, R., Runde, T., Sander, R., Scharffe, D., and Zahn, A.: Earth System Chemistry integrated Modelling (ESCiMo) with the Modular Earth Submodel System (MESSy) version 2.51, Geoscientific Model Development, 9, 1153–1200, https://www.geosci-model-dev.net/9/1153/2016/, 2016.

Jucker, M. and Gerber, E. P.: Untangling the Annual Cycle of the Tropical Tropopause Layer with an Idealized Moist Model, Journal of Climate, 30, 7339–7358, https://doi.org/10.1175/JCLI-D-17-0127.1, 2017.

Jucker, M., Fueglistaler, S., and Vallis, G. K.: Maintenance of the Stratospheric Structure in an Idealized General Circulation Model, Journal of the Atmospheric Sciences, 70, 3341–3358, 2013.

Kerkweg, A., Sander, R., Tost, H., and Jöckel, P.: Technical note: Implementation of prescribed (OFFLEM), calculated (ONLEM), and pseudo-emissions (TNUDGE) of chemical species in the Modular Earth Submodel System (MESSy), Atmospheric Chemistry and Physics, 6, 3603–3609, https://www.atmos-chem-phys.net/6/3603/2006/, 2006.

Lindgren, E. A., Sheshadri, A., and Plumb, R. A.: Sudden Stratospheric Warming Formation in an Idealized General Circulation Model Using Three Types of Tropospheric Forcing. Atmospheres,, Journal of Geophysical Research:, 123(18), 10,125–10,139, 2018.

Liu, Y., Hoskins, B., and Blackburn, M.: Impact of Tibetan Orography and Heating on the Summer Flow over Asia, J. Meteorol. Soc. Jpn., 85B, 1–19, 2007.

Maher, P., Gerber, E. P., Medeiros, B., Merlis, T., Sherwood, S., Sheshadri, A., Sobel, A., Vallis, G., Voigt, A., and Zurita-Gotor, P.: The value of hierarchies and simple models in atmospheric research, Reviews of Geophysics, submitted, 2018.

Nützel, M., Dameris, M., and Garny, H.: Movement, drivers and bimodality of the South Asian High, Atmos. Chem. Phys., 16, 14 755–14 774, http://www.atmos-chem-phys.net/16/14755/2016/, 2016.

5   Pan, L. L., Honomichl, S. B., Kinnison, D. E., Abalos, M., Randel, W. J., Bergman, J. W., and Bian, J.: Transport of chemical tracers from the boundary layer to stratosphere associated with the dynamics of the Asian summer monsoon, Journal of Geophysical Research: Atmospheres, 121, 14,159–14,174, 2016JD025616, 2016.

Polvani, L. M. and Kushner, P. J.: Tropospheric response to stratospheric perturbations in a relatively simple general circulation model, Geophys. Res. Lett., pp. 40–43, 2002.

10   Polvani, L. M., Clement, A. C., Medeiros, B., Benedict, J. J., and Simpson, I. R.: When less is more: Opening the door to simpler climate models, Eos, 98, 2017.

Pozzer, A., Jöckel, P., Kern, B., and Haak, H.: The Atmosphere-Ocean General Circulation Model EMAC-MPIOM, Geoscientific Model Development, 4, 771–784, https://www.geosci-model-dev.net/4/771/2011/, 2011.

Randel, W., Udelhofen, P., Fleming, E., Geller, M., Gelman, M., Hamilton, K., Karoly, D., Ortland, D., Pawson, S., Swinbank, R., Wu,

15   F., Baldwin, M., Chanin, M.-L., Keckhut, P., Labitzke, K., Remsberg, E., Simmons, A., and Wu, D.: The SPARC Intercomparison of Middle-Atmosphere Climatologies, Journal of Climate, 17, 986–1003, 2004.

Randel, W. J. and Park, M.: Deep convective influence on the Asian summer monsoon anticyclone and associated tracer variability observed with Atmospheric Infrared Sounder (AIRS), J. Geophys. Res., 111, D12 314, http://dx.doi.org/10.1029/2005JD006490, 2006.

Sander, R., Jöckel, P., Kirner, O., Kunert, A. T., Landgraf, J., and Pozzer, A.: The photolysis module JVAL-14, compatible with the MESSy

20   standard, and the JVal PreProcessor (JVPP), Geoscientific Model Development, 7, 2653–2662, https://www.geosci-model-dev.net/7/2653/2014/, 2014.

Sander, R., Baumgaertner, A., Cabrera-Perez, D., Frank, F., Gromov, S., Grooß, J.-U., Harder, H., Huijnen, V., Jöckel, P., Karydis, V. A., Niemeyer, K. E., Pozzer, A., Riede, H., Schultz, M. G., Taraborrelli, D., and Tauer, S.: The community atmospheric chemistry box model CAABA/MECCA-4.0, Geoscientific Model Development, 12, 1365–1385, https://www.geosci-model-dev.net/12/1365/2019/, 2019.

25   Schubert, W. H. and Masarik, M. T.: Potential vorticity aspects of the MJO, Dynamics of Atmospheres and Oceans, 42, 127 – 151, http://www.sciencedirect.com/science/article/pii/S037702650600039X, 2006.

Schulzweida, U.: CDO User Guide (Version 1.9.6), https://code.mpimet.mpg.de/projects/cdo/wiki/Cite, 2019.

Siu, L. W. and Bowman, K. P.: Forcing of the Upper-Tropospheric Monsoon Anticyclones, Journal of the Atmospheric Sciences, 76, 1937–1954, 2019.

30   SPARC: SPARC Intercomparison of Middle Atmosphere Climatologies, Edited by W. Randel, M.-L. Chanin and C. Michaut, Tech. rep., SPARC Report No. 3, 2002.

Turner, A. G. and Annamalai, H.: Climate change and the South Asian summer monsoon, Nature Clim. Change, 2, 587–595, http://dx.doi.org/10.1038/nclimate1495, 2012.

Vallis, G. K., Colyer, G., Geen, R., Gerber, E., Jucker, M., Maher, P., Paterson, A., Pietschnig, M., Penn, J., and Thomson, S. I.: Isca, v1.0:

35   a framework for the global modelling of the atmospheres of Earth and other planets at varying levels of complexity, Geoscientific Model Development, 11, 843–859, https://www.geosci-model-dev.net/11/843/2018/, 2018.

Vogel, B., Günther, G., Müller, R., Grooß, J.-U., Hoor, P., Krämer, M., Müller, S., Zahn, A., and Riese, M.: Fast transport from Southeast Asia boundary layer sources to northern Europe: rapid uplift in typhoons and eastward eddy shedding of the Asian monsoon anticyclone, Atmos. Chem. Phys., 14, 12 745–12 762, 2014.

Vogel, B., Günther, G., Müller, R., Grooß, J.-U., and Riese, M.: Impact of different Asian source regions on the composition of the Asian mon-

5   soon anticyclone and of the extratropical lowermost stratosphere, Atmos. Chem. Phys., 15, 13 699–13 716, http://www.atmos-chem-phys. net/15/13699/2015/, 2015.

Wan, H., Giorgetta, M., and Bonaventura, L.: Ensemble Held-Suarez Test with a Spectral Transform Model: Variability, Sensitivity, and Convergence, Monthly Weather Review, 136, 1075–1092, 2008.

Wang, S., Gerber, E. P., and Polvani, L. M.: Abrupt circulation responses to tropical upper-tropospheric warming in a relatively simple

10   stratosphere-resolving AGCM, Journal of Climate, 25(12), 2012.

Wei, W., Zhang, R., Wen, M., Rong, X., and Li, T.: Impact of Indian summer monsoon on the South Asian High and its influence on summer rainfall over China, Clim. Dynam., 43, 1257–1269, http://dx.doi.org/10.1007/s00382-013-1938-y, 2014.

Wei, W., Zhang, R., Wen, M., Kim, B.-J., and Nam, J.-C.: Interannual Variation of the South Asian High and Its Relation with Indian and East Asian Summer Monsoon Rainfall, J. Climate, 28, 2623–2634, http://dx.doi.org/10.1175/JCLI-D-14-00454.1, 2015.

15 Yano, J.-I. and L. McBride, J.: An Aquaplanet Monsoon, Journal of the Atmospheric Sciences, 55, 1373–1399, http://dx.doi.org/10.1175/ 1520-0469(1998)055<1373:AAM>2.0.CO;2, 1998.

Zhang, Q., Wu, G., and Qian, Y.: The Bimodality of the 100 hPa South Asia High and its Relationship to the Climate Anomaly over East Asia in Summer, J. Meteor. Soc. Japan, 80, 733–744, 2002.